Manuscript type: TOOLS

Detection and quantification of the vacuolar H^+-ATPase using the *Legionella* effector protein SidK

Michelle E. Maxson[1], Yazan M. Abbas[2], Jing Ze Wu[1,4], Sergio Grinstein[1,4*] and John L. Rubinstein[2,3,4]

[1] Program in Cell Biology, The Hospital for Sick Children, Toronto, ON M5G 0A4, Canada.

[2] Program in Molecular Medicine, The Hospital for Sick Children Research Institute, Toronto, ON M5G 0A4, Canada.

[3] Department of Medical Biophysics, University of Toronto, Toronto, ON M5G 1L7, Canada.

[4] Department of Biochemistry, University of Toronto, Toronto, ON M5S 1A8, Canada.

Running title: Detection of V-ATPases using SidK

Key words: V-ATPase, SidK, *Legionella*, fluorescence microscopy

[*] Corresponding author: Sergio Grinstein, Program in Cell Biology, The Hospital for Sick Children, 555 University Avenue, Toronto, Ontario, Canada M5G 1X8. Tel.: +1 416 813 5727; Fax: +1 416 813 5727; E-mail: sergio.grinstein@sickkids.ca

ABSTRACT

Acidification of secretory and endocytic organelles is required for proper receptor recycling, membrane traffic, protein degradation, and solute transport. Proton-pumping vacuolar ATPases (V-ATPases) are responsible for this luminal acidification, which increases progressively as secretory and endocytic vesicles mature. An increasing density of V-ATPase complexes is thought to account for the gradual decrease in pH, but available reagents have not been sufficiently sensitive nor specific to test this hypothesis. We introduce a new probe to localize and quantify V-ATPases in eukaryotic cells. The probe is derived from SidK, a *Legionella pneumophila* effector protein that binds to the V-ATPase A subunit. We generated plasmids encoding fluorescent chimeras of $SidK_{1-278}$, and labeled recombinant $SidK_{1-278}$ with AlexaFluor-568 to visualize and quantify V-ATPases with high specificity in live and fixed cells, respectively. We show that V-ATPases are acquired progressively during phagosome maturation, that they distribute in discrete membrane subdomains, and that their density in lysosomes depends on the subcellular localization of the lysosome.

INTRODUCTION

The steady-state pH of individual cellular compartments is a key determinant of their function and must be regulated stringently. Indeed, the luminal pH directs receptor recycling and membrane traffic, regulates protein degradation, and contributes to the transmembrane protonmotive force that drives the transport of a variety of organic and inorganic solutes (Maxfield and McGraw, 2004; Saftig and Klumperman, 2009; Fisher and Scheller, 1988; Huotari and Helenius, 2011). It is therefore not surprising that dysregulation of organellar pH has been implicated in various human diseases such as cancer, neurological disorders, osteoporosis, and autoimmunity (Marshansky et al., 2014; Capecci and Forgac, 2013; Colacurcio and Nixon, 2016; Sun-Wada et al., 2006; Eaton et al., 2021).

Most endocytic and secretory organelles maintain an acidic lumen, with acidification increasing progressively as these organelles approach their terminal stages (Mellman et al., 1986). Thus, the endocytic pathway progresses from slightly acidic early endosomes (pH 6.5) to highly acidic lysosomes (pH 4 to 5). The main driver of organellar acidification is the ATP-dependent proton pump known as the vacuolar H^+-ATPase (V-ATPase). The V-ATPase is present in vesicular membranes of the endocytic and secretory pathways, and is also found in the plasma membrane of specialized cell types involved in the active extrusion of cytosolic protons, such as osteoclasts and renal intercalated cells (Toei et al., 2010; Futai et al., 2019). The V-ATPase is a large rotary complex with 16 different subunits in mammals. ATP-hydrolysis occurs in the soluble catalytic V_1 region (subunits A to H), driving rotation of the enzyme's rotor subcomplex and proton translocation through the V_O regions (subunits a, d, e, f c, c□, ATP6AP1/Ac45, and ATP6AP2/PRR; Abbas et al., 2020). V-ATPase activity is regulated by several mechanisms, including reversible dissociation of the V_1 and V_O regions (Tabke et al., 2014; Kawasaki-Nishi, 2001; Parra and Kane, 1998; Poëa-Guyon et al., 2013), phosphorylation (Voss et al., 2007; Alzamora et al., 2010), and changes in membrane lipid composition (Banerjee et al., 2019; Vasanthakumar et al., 2019; Uchida et al., 1985).

Several parameters determine the steady-state pH of the lumen of an organelle. Because proton pumping by V-ATPase is electrogenic, the rate of pumping can be limited by the permeability of the membrane to neutralizing counter ions. In addition, the accumulation of protons is opposed by ongoing proton backflux or “leak” via a collection of incompletely characterized channels and transporters. A final fundamental parameter is the density of V-ATPase complexes in the membrane of any particular organelle. It has been tacitly assumed that V-ATPase density increases progressively as the components of endocytic and secretory pathways mature and become more acidic. However, this assumption has not been validated for two main reasons. First, it is difficult to isolate individual stages of these pathways with sufficient purity for reliable biochemical analysis. Second, reagents with sufficient resolution and accuracy are lacking for localization and quantification of V-ATPase in cells. Several antibodies to different V-ATPase subunits are available commercially and some of them have yielded satisfactory results in histological analyses, especially of tissues like the kidney where specialized cell types are uniquely enriched in V-ATPases. However, these same antibodies show poor specificity and a low signal-to-noise ratio when used to stain non-specialized single cells, which have a lower abundance of V-ATPases. The interpretation of the resulting immunostaining can be ambiguous, confounding the results.

The paucity and unsatisfactory performance of reagents currently available to study the V-ATPase motivated us to develop a novel tool for its specific intracellular labeling in eukaryotic cells. To this end we took advantage of SidK, an effector protein deployed by *Legionella pneumophila* to inhibit the V-ATPase (Xu et al., 2010). SidK was recently shown to bind directly to yeast and mammalian V-ATPases by (Zhao et al., 2017; Abbas et al., 2020), allowing use of the effector to purify proton pumps from tissue extracts (Abbas et al., 2020). In this study, we describe the generation and labeling of a recombinant fragment of SidK and its use to localize and quantify V-ATPases in eukaryotic cells with high sensitivity and specificity. We utilized this reagent to study the distribution of the V-ATPase in various cell types, and to monitor its

acquisition by membrane-bound compartments as they mature along the endocytic pathway. Lastly, we used SidK to estimate the number of V-ATPase complexes in individual compartments as a function of their position within the cell.

RESULTS

Generation of fluorescent SidK chimeras for expression in mammalian cells

SidK was reported to bind with high affinity to the A subunit of the V-ATPase (Xu et al., 2010; Sharma and Wilkens, 2017; Abbas et al., 2020; Zhao et al., 2017). We reasoned that the *Legionella* effector would be an effective probe to visualize V-ATPase by fluorescence microscopy. To this end we generated chimeric constructs consisting of amino acids 1 to 278 of SidK ($SidK_{1-278}$) attached to a fluorescent protein (GFP or mCherry) with a linker sequence. $SidK_{1-278}$ suffices to interact with the A subunit with high specificity; indeed, this fragment was used for the affinity purification of V-ATPases from cell and tissue extracts (Fig. 1A; see also Abbas et al., 2020). GFP or mCherry were linked to $SidK_{1-278}$ via its C terminus because the structure of the V-ATPase:$SidK_{1-278}$ complex suggested that attachment at this position was unlikely to affect association of the chimera with the V-ATPase (Fig. 1B; Abbas et al., 2020). For brevity, the resulting construct is referred to simply as SidK.

As is often the case, varying levels of expression were observed following transient transfection of fluorescent SidK in HeLa cells. The fluorescence intensity of the soluble (excess) SidK seen in high expressers ($SidK_{high}$) precluded the resolution of the fraction of the construct bound to V-ATPase-containing organelles, such as lysosomes (Fig. 1C). In contrast, SidK showed clear association with vesicular and tubular structures in low-expressing cells ($SidK_{low}$, Fig. 1D), some of which were identifiable as lysosomes by loading with fluorescent dextran. Because the excess fluorescence of $SidK_{high}$ cells appeared to be cytosolic, we predicted that selective removal of soluble material would reveal the more tightly-bound, organelle-associated probe. This assumption was tested by comparing $SidK_{high}$ cells before (Fig. 1E) and after (Fig.

1F) selective leaching of cytosolic components following permeabilization of the plasma membrane with the pore-forming toxin, pneumolysin (PLY). As anticipated, the cytosolic fluorescence was largely depleted in PLY-treated cells, revealing membrane-associated SidK, a fraction of which was clearly co-localized with LAMP1, a marker of late endosomes/lysosomes. We concluded that the fluorescent chimeras of SidK can be used for detection of membrane-associated ligands, presumably V-ATPases, particularly in cells with low expression level or permeabilized with PLY or similar reagents.

Expression of SidK-fluorescent protein constructs affects lysosomal positioning and pH

In otherwise untreated HeLa cells late endosomes/lysosomes are largely located near the nucleus, as revealed by LAMP1 immunostaining (Fig. 2A). However, we noted that endo/lysosomes tended to accumulate at the cell periphery of SidK-transfected cells, particularly those where the construct was highly expressed (Fig. 2B; see also 1F). Because SidK has been shown to inhibit the V-ATPase partially both *in vitro* and in mammalian cells (Zhao et al., 2017; Xu et al., 2010), we considered the possibility that inhibition of proton pumping was responsible for the altered distribution of LAMP1-positive compartments. This notion was validated by treating cells with concanamycin A, a potent and specific V-ATPase inhibitor, which resulted in a similar margination of a fraction of the LAMP1-positive compartments (Fig. 2C). These observations are consistent with previous reports that the positioning of lysosomes correlates with their luminal pH (Johnson et al., 2016).

To verify that SidK caused lysosomal alkalinization we used cresyl violet (Ostrowski et al., 2016), an acidotropic fluorescent dye that is more photostable than the LysoTracker dye used by Xu et al. (2010). Unexpectedly, and in apparent disagreement with the findings of Xu et al. (2010), the lysosomes remained acidic (retained cresyl violet) despite the presence of SidK in the cytosol (Fig. 2D). The reliability of cresyl violet as an indicator of lysosomal acidification was confirmed using concanamycin A, which prevented the accumulation of the acidotropic dye (Fig.

2E). It is noteworthy, however, that like other acidotropic dyes, cresyl violet is a coarse indicator of pH, unable to sense moderate changes in pH. In this regard, it is of interest that *in vitro* determinations using purified yeast V-ATPase showed that saturating concentrations of SidK caused only a ≈30% inhibition of ATPase activity (Zhao et al., 2017). To more precisely assess the effect of SidK expression on HeLa cells, their lysosomes were loaded with FITC-dextran and pH was measured ratiometrically *in situ* (see Materials and Methods). Using this approach, the pH of lysosomes in SidK-expressing cells was found to be moderately –yet significantly– more alkaline (pH 5.22 ± 0.12) than that of control cells (pH 4.97 ± 0.07; Fig. 2F). As discussed above, a variety of parameters influence the steady-state luminal pH of an organelle. Therefore, we endeavored to more directly assess the effect of SidK on proton pumping by the V-ATPase. This activity can be measured by quantifying the effect of concanamycin on proton flux across the lysosomal membrane. These measurements are based on the assumption that at steady-state pH, V-ATPase activity is precisely offset by an equivalent but opposite backflux (leak) of protons. The initial rate of proton leakage unmasked by addition of saturating concentrations of concanamycin can therefore be considered as an accurate measure of proton pumping by the V-ATPase at steady-state. This analysis (Fig. 2G) indicated that SidK reduced proton pumping by the V-ATPase by 29%, in good agreement with previous *in vitro* measurements (Zhao et al., 2017). Whether the modest change in pH or the more obvious inhibition of the rate of pumping are responsible for the redistribution of lysosomes within the cells remains to be established.

Localization of the V-ATPase in mammalian cells using SidK-AL568

The preceding results indicated that, while capable of detecting the V-ATPase under appropriate conditions, expression of a genetically-encoded form of fluorescent SidK had obvious limitations, most notably the fact that chronic inhibition of the pump –even if only partial– alters the distribution of the labeled organelles. To avoid inhibition of the pump prior to its detection we developed an alternative probe based on SidK that could be used to label the

V-ATPase in fixed and permeabilized cells. Recombinant $SidK_{1-278}$ was expressed in bacteria and, after purification to near homogeneity (Fig. 1A), was covalently labeled with Alexa Fluor 568 (referred to hereafter as SidK-AL568) and used to stain cells. In HeLa cells, SidK-AL568 labelled vesicular and cisternal compartments reminiscent of endosomes and the Golgi complex with remarkably little background noise (Fig. 3A, left panel). This staining was blocked by pretreatment with unlabeled SidK (Fig. 3A, right panel), implying that binding is saturable and that Alexa Fluor conjugation did not alter the binding properties of SidK.

The specificity of SidK-AL568 for the A subunit of the V-ATPase was validated by comparing staining of wild-type *Saccharomyces cerevisiae* to that of a mutant strain lacking the gene for subunit A (*vma1*Δ). SidK-AL568 clearly labeled the vacuole and pre-vacuolar compartment of wild-type spheroplasts, but staining was absent in the *vma1*Δ strain. Additional evidence that SidK-AL568 associates with assembled V-ATPase complexes in mammalian cells was obtained by ectopic (over)expression in HeLa cells with fluorescently tagged V_oa2 or V_oa3 subunits that localize predominantly to the Golgi complex or endosomes, respectively (Saw et al., 2011). SidK-AL568 co-localized with both V_oa2- and V_oa3-GFP, with highly significant Manders' coefficients (M= 0.74 and 0.79, respectively; Figs. 3C and D). Taken together, these data verified that fluorescently labeled SidK is a sensitive tool for the specific detection of the V-ATPase in eukaryotic cells, where it detects primarily organelle-associated complexes.

We proceeded to use SidK-AL568 to assess the presence and density of V-ATPase complexes in defined intracellular compartments, an experiment that –while conceptually simple– has been hampered by the paucity of sufficiently sensitive reagents. As intimated above and illustrated in more detail in Fig. 4A, SidK-AL568 stained peripheral vesicular compartments (Fig. 4A, open arrowheads) as well as juxtanuclear vesicles and cisternae (closed arrowheads) likely corresponding to endocytic and Golgi components, respectively. These assumptions were confirmed by simultaneously visualizing LAMP1 and the *trans*-Golgi (Figs. 4B and C), demonstrating that SidK-AL568 staining has a high degree of colocalization with these

compartments, which are known to have a markedly acidic lumen (Casey et al., 2009). In contrast, SidK-AL568 showed minimal colocalization with markers of the endoplasmic reticulum (ER) and mitochondria (Figs. 4E and F), which have a near-neutral or slightly alkaline lumen (Casey et al., 2009). Of note, SidK-AL568 labeled poorly the *cis*-Golgi (Fig. 4D), which is thought to be less acidic than the *mid*- and *trans*-cisternae.

Based on the previous observations, we believe that SidK-AL568 is an excellent probe to detect V-ATPase, possibly superior to other reagents commonly used in the literature. Indeed, when compared to a commercially available antibody raised against the same subunit to which SidK-AL568 binds (V-ATPase subunit A), our probe yielded better results. The antibody chosen for comparison (α-ATP6V1A) is widely used in the literature to document the localization of V-ATPases, often as the basis to reach important functional conclusions (e.g. Ramirez et al., 2019). When tested in HeLa cells (Figs. 4G and H), this antibody yielded a diffuse punctate pattern reminiscent of that reported by Ramirez et al. (2019) for tumour cells and elsewhere for a variety of other cells stained with other A subunit antibodies (Yajima et al., 2007; McGuire et al., 2019; Michel et al., 2013). However, its co-localization with acidic compartments was poor: the Manders' coefficient of the antibody with LAMP1 was M = 0.08 (compared to an M = 0.79 with SidK-AL568), while that with anti-TGN46, the *trans*-Golgi marker used, was M = 0.05 (compared to an M = 0.81 with SidK-AL568). Comparison of the α-ATP6V1A signal with that of SidK-AL568 showed that most of the α-ATP6V1A staining was background, which was removed by applying the unbiased Costes thresholding method prior to colocalization analysis (Costes et al., 2004); see Materials and Methods); this was not the case for SidK-AL568 staining (Fig. S1). We therefore suggest that SidK-AL568 is a more specific, preferable probe.

Assessment of V-ATPase acquisition by maturing phagosomes

The phagosomes formed by cells of the innate immune system, such as macrophages, are specialized compartments with microbicidal and degradative functions. The lumen of nascent phagosomes is near-neutral, but becomes gradually acidic as the compartment matures, reaching a pH ≤ 5 (e.g. Fig. 5A). This acidification has been demonstrated to depend on the activity of V-ATPases (Lukacs et al., 1990), which are nevertheless undetectable on the macrophage plasma membrane that forms the initial phagosomal enclosure. The graded acidification is thought to result from accumulation of V-ATPases complexes owing to fusion of the nascent phagosome with early and late endosomes and, ultimately, with lysosomes. Remarkably, to our knowledge, this purported mechanism has not been documented experimentally. We therefore utilized the SidK-AL568 probe to detect V-ATPases during the phagosomal maturation process, using murine macrophages (RAW264.7 cells) that had been transfected with various membrane markers correlated to maturation state (Fig. 5B).

Like HeLa cells, resting RAW264.7 macrophages showed distinct vesicular staining with SidK-AL568, as well as larger vacuoles that likely form by macropinocytosis, which is constitutively active in these cells (Fig. 5C). Nascent phagosomes, enriched by arresting phagocytosis shortly (2 min) after exposure to the target particles, were identified by the persistence of plasmalemmal markers (e.g. PM-GFP). As expected, these nascent phagosomes were essentially devoid of V-ATPases, although V-ATPase-rich organelles seemed to accumulate in their immediate vicinity (Fig. 5D). In contrast, early phagosomes –which are measurably acidic and were identified by the acquisition of Rab5 and PtdIns(3)P– showed distinct acquisition of SidK-AL568 into discrete areas (Fig. 5E and F). Late phagosomes/phagolysosomes, which were identified by possessing Rab7 or LAMP1, were even more enriched with SidK-AL568 (Fig. 5G and H), consistent with their highly acidic pH. Interestingly, a patchy localization of SidK-AL568 was noted at all stages of phagosome maturation, suggesting that the recruitment of V-ATPases may occur at restricted sites, which may have important implications for traffic and pH regulation.

247

248 **The V-ATPase is heterogeneously distributed on the membrane of acidic organelles**

249 The discontinuous pattern of SidK-AL568 on the late-phagosome membrane is reminiscent
250 of the spatial segregation of other membrane components that was observed previously and
251 associated with the formation of ER-phagosome contacts (Levin-Konigsberg et al., 2019).
252 These contacts are established, at least partly, by interaction of phagosomal ORP1L with the
253 ER resident proteins VapA and VapB (Rocha et al., 2009; Loewen and Levine, 2005). We
254 considered the possibility that the SidK-AL568 patches represented similar regions of V-ATPase
255 exclusion from ER contact sites. To assess this possibility, phagosomes of RAW264.7 cells that
256 had been transfected with ORP1L-GFP were stained with SidK-AL568. Following transfection
257 (Fig. 6A), ORP1L and the V-ATPase showed an inverse distribution, the latter accumulating in
258 regions where the former was depleted. This segregation could be quantified and is represented
259 as a ratio of SidK-568:ORP1L fluorescence in the rightmost panel of Fig. 6A. In contrast, SidK-
260 AL568 co-distributed with Arl8b (Fig. 6B), which was shown earlier to be excluded from ER
261 contact sites (Levin-Konigsberg et al., 2019). It was imperative to ensure that the apparent
262 depletion of V-ATPases from contact areas was not caused by limited access of SidK-AL568.
263 Accessibility was verified by immunostaining VapB alongside SidK-AL568 (Fig. 6C). As was the
264 case for ORP1L, the regions that were rich in VapB were comparatively depleted of SidK-
265 AL568. Because the antibody used to immunostain VapB is much larger (≈150 kDa) than SidK-
266 AL568 (≈35 kDa), exclusion of the V-ATPase ligand cannot account for the observed
267 segregation, which is an indication of the genuine existence of V-ATPase-enriched
268 microdomains.

269 The realization that unappreciated microdomains rich in V-ATPases exist in phagosomes
270 prompted us to ask whether similar subdomains exist in other organelles. To facilitate
271 visualization, we initially generated enlarged lysosomes using sucrose (Cohn and Ehrenreich,
272 1969; Bright et al., 1997; DeCourcy and Storrie, 1991; Swanson et al., 1986; Ferris et al., 1987)

in cells that had been transfected with ORPL1 (Fig. 7A) or Arl8b (Fig. 7B). As with late phagosomes, V-ATPase (SidK-AL568) was depleted from membrane domains where ORPL1 was found, while coinciding with Arl8b.

In addition to visualizing V-ATPase microdomains in enlarged phagosome or sucrose-enlarged lysosomes, the existence of comparatively long tubular lysosomes in macrophages also enabled us to assess segregation in resting, unmodified cells. In RAW264.7 macrophages (Fig. 7C) and human monocyte-derived macrophages (Fig. 7D), regions of late endosome/lysosomes –identified by LAMP1– were preferentially enriched with V-ATPase. This pattern could also be observed in some HeLa cells where the LAMP1-positive structures were sufficiently large (Fig. 7E). In all cases, regions of V-ATPase exclusion from LAMP1-stained areas were observed; in some instances SidK-AL568- stained structures appeared to bud off from LAMP-positive tubular lysosomes. The observed segregation may be an indication of selective delivery or removal of V-ATPases at varying stages of organellar maturation.

Quantification of the number of V-ATPases per lysosome: evidence of heterogeneous density that correlates with the subcellular localization of the organelles

To date, estimates of the number of V-ATPase complexes in vesicular compartments have been global approximations based on measurements made in pooled whole-cell preparations (de Araujo et al., 2020; Takamori et al., 2006). In an effort to refine estimates and provide topological information, we attempted to quantify the number of SidK-AL568 molecules bound per organelle. This analysis required determination of the fraction of SidK molecules labeled by the Alexa dye and the number of fluorophores attached per SidK-AL568 molecule, followed by comparison of the single molecule fluorescence to the total fluorescence associated with the organelle of interest. We determined that 96.7% of the molecules were labeled and analysis of the photobleaching pattern of monodisperse SidK (Fig. 8A; see Materials and Methods) indicated that 99% of these molecules had reacted with a single fluorophore (Fig. 8B).

We next determined the concentration of SidK-AL568 needed to saturate all the available binding sites on lysosomes (Fig. 8C). With these parameters and conditions, the total fluorescence associated with individual lysosomes was converted to a corresponding number of V-ATPases, with the assumption that all three A subunits of every V-ATPase are accessible for SidK-AL568 binding. In HeLa cells, where individual lysosomes can be delineated more readily than in macrophages, the number of SidK-AL568 molecules associated per lysosome varied (Fig. 8D), with an average of 4.42 ± 0.03 (mean ± SEM) SidK molecules per lysosome, equivalent to 1.47 V-ATPase complexes per lysosome.

Previous research had shown that lysosomes are heterogeneous within a cell (Bright et al., 1997, 2016; Butor et al., 1995; Cheng et al., 2018). Additionally, lysosomal pH can vary with vesicle positioning, with peripheral lysosomes generally being more alkaline, and lysosomes near the center of the cell being more acidic (Johnson et al., 2016; Webb et al., 2021). A simple explanation for this finding could be that peripheral lysosomes have fewer V-ATPase complexes than central lysosomes, although other mechanisms could also cause this effect (see Introduction). To explore this phenomenon experimentally, lysosomes of HeLa cells were identified with LAMP1 as a marker and their V-ATPase density quantified with SidK-AL568. The resultant labeling with SidK-AL568 was more intense in juxtanuclear lysosomes than in more peripheral lysosomes (Fig. 8E). This differential distribution was quantified and is represented as a ratio of SidK-AL568:LAMP1 fluorescence (Fig. 8F). To more precisely assess whether the number of V-ATPases per lysosome varies as a function of their subcellular localization, the SidK-AL568 fluorescence of individual LAMP1-positive structures was analyzed relative to their distance from the edge of the cell. Cell outlines were drawn and degraded inward by 4 μm iteratively, to create concentric shells within each cell (Fig. 8G). Comparison of these subgrouped LAMP1-positive vesicles confirmed the existence of a gradient of SidK-AL568 that correlates with the distance of the lysosomes from the cell center. The most juxtanuclear lysosomes bind approximately twice as many SidK-AL568 molecules as peripheral ones (Fig.

8H). This change in V-ATPase density corresponded to 2.1 V-ATPase complexes per lysosome at >16 µm from the cell edge, compared to 1.1 lysosomal V-ATPases per lysosome for lysosomes 0 to 4 µm from the cell edge. Interestingly, ≈18% of the lysosomes closest to the nucleus showed more than the average number of V-ATPase complexes (2 to 6 per lysosome). We conclude that the pH heterogeneity of lysosomes within individual cells can be explained, at least in part, by differences in their V-ATPase density.

DISCUSSION

Despite its clear importance in the maintenance of organellar pH and tissue homeostasis, the study of V-ATPases has been hampered by the lack of reagents to accurately localize and quantify these complexes. To address this problem, we developed a detection tool based on SidK, a *L. pneumophila* effector protein. SidK was an attractive detection tool for several reasons. First, it was reported to bind to the V-ATPase A subunit with high specificity (Abbas et al., 2020; Zhao et al., 2017; Xu et al., 2010) and affinity; SidK binds to the V-ATPase with a $K_d \approx$ 3.5 nM (Sharma and Wilkens, 2017), which is comparable to the affinity of many immunoglobulins for their cognate antigens. Second, because the primary sequence of the V-ATPase A subunit is highly conserved across Eukarya, a SidK-based reagent should be applicable to a variety of model organisms. Indeed, we found SidK to interact equally with yeast and mammalian cells. Finally, unlike other V-ATPase subunits, the A subunit exists as a single isoform, so that the SidK reagent would be expected to bind V-ATPase wherever present in organelles, cells, and tissues.

We first expressed the V-ATPase-binding region of SidK (amino acids 1 to 278) as a fusion with GFP or mCherry. At modest expression levels, this construct enabled the detection of V-ATPase-rich membranes. However, at higher expression levels the unbound (cytosolic) probe obscured the intracellular organelles. This problem could be mitigated by leaching the cytosolic excess out the cells by permeabilizing the plasmalemma with PLY, revealing the specifically-

bound constructs. However, when expressing SidK, a process that requires hours, we observed a change in lysosomal positioning that we attributed to its inhibitory effect, as it mimicked the effects of concanamycin A. Accordingly, we measured a ≈ 30% inhibition of the proton-pumping rate in cells expressing SidK-mCherry. While our findings were not unexpected considering the observations made earlier *in vitro* and in cells (Abbas et al., 2020; Zhao et al., 2017; Xu et al., 2010; Johnson et al., 2016), they nonetheless underscored a limitation inherent to the use of ectopically expressed SidK. Indeed, inhibition of V-ATPase and the resultant changes in luminal pH can affect not only lysosome localization, but also the ability of the V-ATPase to interact with other molecules (Maranda et al., 2001; Hurtado-Lorenzo et al., 2006; Hosokawa et al., 2013), altering intracellular signaling (Balgi et al., 2011; Hu et al., 2016). In this context, it is noteworthy that SidK-GFP/mCherry did not properly label acidic portions of the Golgi complex. This lack of labeling could have resulted from obstruction caused by other molecules that associate with V-ATPase in the Golgi, but not with those of the endocytic compartment.

To circumvent the problems associated with SidK expression, we utilized fluorescently-conjugated recombinant SidK as an overlay staining reagent, followed by washing to remove unbound probe. SidK-AL568 localized to punctate and cisternal structures in mammalian cells, with little nonspecific background. The high signal-to-noise ratio, along with specific organellar markers allowed us to clearly discern V-ATPase-positive organelles, primarily endo/lysosomes and the *trans*-Golgi. This labeling was in sharp contrast to the staining we obtained using a commercially available antibody to the A subunit and the conditions for its use described in the literature (Ramirez et al., 2019), which yielded results similar to those reported by others using other available antibodies (Yajima et al., 2007; McGuire et al., 2019; Michel et al., 2013). V-ATPase complexes have been shown to interact with several accessory proteins involved in endocytic sorting and signaling (Merkulova et al., 2015; Maxson and Grinstein, 2014; Marshansky et al., 2014). These interacting proteins include sorting nexins SNX27, SNX10 and SNX11 (Merkulova et al., 2015; Chen et al., 2012; Xu et al., 2020), and the Ragulator complex,

which controls mTOR activation during nutrient sensing (Zoncu et al., 2011). Additionally, the V-ATPase is hypothesized to function as a sensor of luminal pH, that regulates endocytosis through a pH-dependent interaction with ARNO, the guanine nucleotide exchange factor for Arf6 (Hosokawa et al., 2013; Maranda et al., 2001; Hurtado-Lorenzo et al., 2006). Recently, some members of TLDc protein family have been found to interact with V-ATPase domains and modulate V-ATPase activity or stability (Merkulova et al., 2015; Castroflorio et al., 2021). These reports have relied on immunoprecipitation with available V-ATPase antibodies to study interactions. However, use of the more specific SidK-AL568 probe could provide more sensitive and/or specific measurements of interactions, as well as the ability to visualize novel interactions by high-resolution microscopy. Of interest, the 34.6 kDa $SidK_{1-278}$ fragment we used is considerably smaller than conventional primary antibodies (IgG ≈150 kDa), which are often used in combination with an equally large secondary antibody. Our smaller probe is better suited to access V-ATPases, and could therefore be advantageous for immunogold-labeling for transmission electron microscopy, where the penetrance of bulky antibodies can limit detection. The smaller size of SidK-AL568 compared to SidK-GFP/mCherry may also explain why the former is better able to detect V-ATPase in the Golgi complex, although fixation and permeabilization may have also facilitated its access.

The successful labeling of the acidic intracellular compartments emboldened us to utilize the probe to monitor the dynamics of recruitment of the V-ATPase to a specialized vesicular compartment, the phagosome. The progressive development of phagosomal acidification is well established and was assumed, yet not proven, to be associated with increasing V-ATPase density. We found that while the nascent phagosome is virtually devoid of V-ATPases, the presence of the complex becomes evident in early (Rab5- and PtdIns(3)P-positive) phagosomes, and their number increases further as they attain the phagolysosomal stage. Therefore, the increasing acidity during maturation can be attributed, at least in part, to an increase in V-ATPase density. This increase in density correlates well with the recent finding

that acidification of phagosomes to a pH < 6 during the transition between early and late phagosome results in the dissociation of Vps34 class III phosphatidylinositol-3-kinase from these organelles (Naufer et al., 2018). Therefore, V-ATPase recruitment to the phagosome would be expected to control the cessation of PtdIns(3)P synthesis on these compartments, which is necessary for transition to the late phagosome/phagolysosome stage (Vieira et al., 2001; Naufer et al., 2018).

We also observed that V-ATPase was not homogeneously localized throughout the membrane of the phagosome, and similar observations were made in enlarged and normal lysosomes. The existence of specialized subdomains was recently reported in phagosomes, where it was associated with the formation of contacts with the ER and the extension of tubular structures (Levin-Konigsberg et al., 2019). In the endocytic system, similar microdomains have been postulated to play roles in cargo sorting and receptor recycling through tubulation (Wijdeven et al., 2016; Rocha et al., 2009), and are likely also involved in phagosome resolution. Once internalized material has been degraded by acidic hydrolases, essential phagosomal and lysosomal membrane proteins must be parsed and redistributed within the cell for reutilization. The reformation of the lysosomal compartment by membrane-retrieval following content condensation was predicted long ago (Bright et al., 1997, 2016; Mullock et al., 1998), but the fate of specific components has not been well documented. In the case of the V-ATPase, retrieval from maturing phagosomes was demonstrated in *Dictyostelium discoideum* (Clarke et al., 2010), but to our knowledge has not been studied in mammalian cells. The observed V-ATPase-rich domains may be a precursor to the formation of recycling vesicles or tubules. In this regard, pH gradients have been recently observed in tubules formed by macrophages (Suresh et al., 2020; Naufer et al., 2018). Taken together, these findings suggest that proton-pumping microdomains may form on acidic organelles during the tubulation and fission that accompany resolution.

The high signal-to-noise ratio provided by the SidK-AL568 probe and its defined labeling stoichiometry enabled us to quantify the number of V-ATPase complexes per organelle. Quantification relied on the use of saturating concentrations of the probe, a requirement that was fulfilled by analyzing the concentration dependence of SidK-AL568 binding. We calculated the number of V-ATPases per lysosome to range between 1 and 6, averaging ≈1.5. This number is similar to estimates for synaptic vesicles, with one V-ATPase per vesicle (Takamori et al., 2006). The paucity of pumps per organelle likely accounts for the difficulty encountered in their detection and highlights the need for highly-specific probes. It is important to emphasize that our estimates for the number of V-ATPases rely on the assumption that all three A subunits of every pump are accessible to the probe. Because an increasing number of proteins are appreciated to bind to the V-ATPase, steric hindrance may curtail the number of available subunits, which would result in an underestimate of the number of pumps. Through these experiments, we noted that the distribution of V-ATPases in association with LAMP1-positive structures was not homogeneous throughout the cell: more SidK-AL568 bound to juxtanuclear lysosomes, when compared to peripheral lysosomes. Shell analysis showed that the density of SidK-AL568 increased with distance from the cell edge, with the most central lysosomes containing up to 6 V-ATPases. These data are in line with recent reports showing that juxtanuclear lysosomes are, on average, more acidic than the more peripheral ones (Johnson et al., 2016; Webb et al., 2021).

While bearing in mind the caveats raised above regarding the assumption of unimpeded access to all the A subunits, our estimates can be used to calculate the rate of pumping of individual lysosomal V-ATPases *in situ*. Experiments like those in Fig. 2H indicated that addition of concanamycin alkalinized the lysosomes at an initial rate of 0.198 ± 0.1 $pH.min^{-1}$. Because at steady state the activity of the pumps must have matched the proton leak unmasked by concanamycin, the measured rate can be used to estimate pump activity. Considering the buffering power of the lysosomes, which we estimated to be 23.5 $mM.pH^{-1}$ –measured by

pulsing with ammonium– we calculate a proton flux per lysosome volume of 9.50×10^{-2} $mmol.min^{-1}.L^{-1}$. Assuming an approximate lysosomal volume of $2 \times 10^{-17}.L^{-1}$ (de Araujo et al., 2020; Yordanov et al., 2019), this measurement is equivalent to a flux of 953 $H^{+}.sec^{-1}$ per lysosome. As ten protons are pumped by the V-ATPase for every three ATPs hydrolyzed (Zhao et al., 2015), the flux corresponds to approximately 191 molecules of ATP hydrolyzed per lysosome per sec. Considering that there are 1 to 2 pumps on average per lysosome, the calculated flux is within the same order as the V-ATPase activity measured previously in cell-free systems in mammals (29.2 ATP per V-ATPase.sec^{-1}; Abbas et al., 2020) and yeast (from 3.7-300 ATP per V-ATPase.sec^{-1}; Vasanthakumar et al., 2019; Uchida et al., 1985; Sharma and Wilkens, 2017; Kawasaki-Nishi, 2001). The rate estimated here in intact cells may differ from some of the *in vitro* measurements due to the effect of regulatory factors and parameters, such as availability of counterions, phosphorylation, membrane lipid composition, etc. that are not encountered in cell-free enzyme assays.

In summary, we have introduced a new, powerful probe to visualize and quantify V-ATPases in eukaryotic cells. This probe enabled us to assess the subcellular distribution of V-ATPases and, in combination with ratiometric pH determinations, estimate the rate of flux for individual lysosome-associated V-ATPase complexes in intact cells. These results reveal heterogeneity in the lysosomal compartment that is a result of vesicle location dependent differences in V-ATPase density. We also expect this probe to be a useful label for super-resolution imaging and electron microscopy, and anticipate that SidK-AL568 and similar SidK-derived probes will contribute not only to studies of V-ATPase complexes in cells, but to our understanding of endocytic and secretory processes more generally.

MATERIALS AND METHODS

Cell culture

HeLa and RAW264.7 cells were obtained from and authenticated by the American Type Culture Collection (ATCC). Both cell lines tested negative for mycoplasma contamination by DAPI staining. HeLa cells were grown in DMEM containing L-glutamine and 10% heat-inactivated fetal calf serum (FCS; MultiCell, Wisent) at 37°C under 5% CO_2. RAW264.7 cells were grown in RPMI-1640 medium containing L-glutamine and 10% heat-inactivated FCS, at 37°C under 5% CO_2.

To obtain non-polarized human monocyte-derived macrophages (M0 hMDMs), peripheral blood mononuclear cells (PBMCs) were isolated from the blood of healthy donors by density-gradient separation with Lympholyte-H (Cedarlane). Human monocytes were then separated by adherence and incubated in RPMI-1640 containing L-glutamine, 10% heat-inactivated FCS, 100 $U.mL^{-1}$ penicillin, 100 $\mu g.mL^{-1}$ streptomycin, 250 $ng.mL^{-1}$ amphotericin B and 25 $ng.mL^{-1}$ hM-CSF (PeproTech) for 5 to 7 days, at 37ºC under 5% CO_2, before experimentation.

Reagents

Mammalian expression vectors were obtained from the following sources: pmCherry-N1 (Clontech) and pEGFP-N1 (Clontech), sec61b-GFP (Addgene; plasmid no. 121159), PM-GFP (Teruel et al., 1999), Rab5A-GFP (Roberts et al., 2000), PX-GFP (Kanai et al., 2001), Rab7-GFP (Bucci et al., 2000), LAMP1-GFP (Martinez et al., 2000), ORP1L-GFP (Rocha et al., 2009), Arl8b-GFP (Johnson et al., 2016). V_Oa1-, V_Oa2-, and V_Oa3-GFP were the kind gift of Dr. Shuzo Sugita (UHN, Toronto).

Primary antibodies were purchased from the following vendors: anti-human LAMP1 (Developmental Studies Hybridoma Bank; catalogue no. H4A3-s), anti-VapB (Sigma-Aldrich;

503 catalogue no. HPA013144), anti-TGN46 (Abcam; catalogue no. ab50595), anti-GM130 (BD
504 Transduction Laboratories; catalogue no. 610822), anti-V1A (Abnova; catalogue no.
505 H00000523-M02). Secondary antibodies conjugated with Alexa Fluor-405, -488, -555 or -647
506 were purchased from Jackson ImmunoResearch Labs.
507 Fluorescently-conjugated 10 kDa dextrans, Alexa Fluor-405 and Alexa Fluor-568 NHS
508 esters, and fluorescently conjugated phalloidin and streptavidin were purchased from Invitrogen.
509 Concanamycin A, nigericin, DAPI, propidium iodide and cresyl violet were from Sigma-Aldrich.
510 Sheep red blood cells (SRBC; 10% suspension) were from MP Biomedicals. Anti-sheep red
511 blood cell antibodies were from Cedarlane Laboratories. Paraformaldehyde (PFA; 16% wt/vol)
512 was from Electron Microscopy Sciences.
513
514 **SidK-GFP/mCherry plasmid construction**
515 SidK$_{1-278}$ was amplified by PCR using plasmid pSAB35 (Abbas et al., 2020) as a
516 template, with the following forward and reverse primers, respectively: 5´-
517 GAGGAGGAATTCATGTCTTTTATCAAGGTAGGTATAAAAATG-3´ and 5´-
518 GAGGAGGGATCCCCTTTGCTTAAAGCATTTAATTTTTCG-3´. The PCR product was digested
519 with EcoRI and BamHI (New England Biolabs), and ligated into pmCherry-N1 and pEGFP-N1
520 plasmids that had been digested with the same restriction enzymes.
521 For illustrative purposes, a model of yeast V-ATPase with SidK-GFP bound (Fig. 1B)
522 was generated from PDB accession no. 5VOX, 1GFL and 6O7T, using *UCSF ChimeraX*
523 (Goddard et al., 2018).
524
525 **Purification of SidK$_{1-278}$ protein**
526 To purify SidK$_{1-278}$-3×FLAG, *Escherichia coli* strain BL21 was transformed with pSAB35
527 (Abbas et al., 2020) and grown at 30°C with shaking in 1 L LB medium (BioShop) supplemented
528 with 50 mg.L^{-1} kanamycin. At an OD$_{600}$ of 0.6-0.8, protein expression was induced with 1 mM

529 IPTG and cells grown overnight at 16°C. All subsequent steps were performed at 4°C. Cells
530 were harvested by centrifugation at 5,250 ×*g*, resuspended in 25 mL HisTrap Buffer (50 mM
531 Tris-HCl pH 7.4, 25 mM imidazole, and 300 mM NaCl) and lysed by sonication. The cell lysate
532 was centrifuged at 38,000 ×*g* and the supernatant was loaded onto a 5 mL HisTrap Ni-NTA
533 column (GE Healthcare). The column was washed with HisTrap Buffer and protein eluted with a
534 linear gradient of imidazole from 25 to 300 mM in HisTrap Buffer over 10 column volumes.
535 Fractions containing 6×his-SidK$_{1-278}$-3×FLAG were pooled, mixed with TEV protease,
536 and dialyzed against 2 L Dialysis Buffer (50 mM Tris-HCl pH 7.4 and 300 mM NaCl) with 1 mM
537 dithiothreitol (DTT) overnight. Cleaved protein was dialyzed against 2×1 L Dialysis Buffer to
538 remove imidazole and DTT and passed through a 5 mL HisTrap column. The column was
539 washed with HisTrap Buffer and the flowthrough and wash were collected, pooled, and
540 concentrated in a centrifugal concentrating device (EMD Millipore). To remove aggregated
541 protein, SidK$_{1-278}$-3×FLAG was further purified with a Superdex 200 10/300 Increase gel filtration
542 column (GE Healthcare) equilibrated with 50 mM Tris-HCl pH 7.4 and 150 mM NaCl. Fractions
543 containing protein were pooled, concentrated, flash-frozen in liquid N_2, and stored at -80°C.
544
545 **Purification of *Saccharomyces cerevisiae* V-ATPase using SidK**
546 *Saccharomyces cerevisiae* strain BJ2168 was grown in 11 L yeast extract peptone
547 dextrose medium (YPD; BioShop) in a Microferm fermenter (New Brunswick Scientific) at 30°C,
548 with aeration of 34 cubic feet per hour, and stirring at 300 rpm. Yeast were harvested after 18 h
549 (OD_{660} = 4.5) by centrifugation at 4,000 x*g* for 15 min at 4°C. All subsequent steps were
550 performed at 4°C. Cell walls were broken by bead beating in lysis buffer (phosphate-buffered
551 saline, pH 7.4, 8% (w/v) sucrose, 2% (w/v) sorbitol, 2% (w/v) glucose, 5 mM □-aminocaproic
552 acid, 5 mM *p*-aminobenzoic acid, 5 mM EDTA, and 0.001% (w/v) PMSF). Cellular debris was
553 removed by centrifugation at 3,000 x*g* for 10 min and cell membranes were collected by

554 ultracentrifugation at 152,957 x*g* for 40 min. The membrane pellet was resuspended in 36 mL
555 lysis buffer, divided into 4 aliquots, flash-frozen in liquid N_2, and stored at -80°C. Two membrane
556 pellets (corresponding to half a fermenter growth) were thawed and solubilized with addition of
557 n-dodecyl-β-D-maltopyranoside (DDM, Anatrace) to 1% (w/v) final concentration, and DDM-
558 solubilized *S. cerevisiae* V-ATPase isolated with M2 Affinity agarose gel (Sigma-Aldrich) pre-
559 loaded with $SidK_{1-278}$-3×FLAG as described previously (Abbas et al., 2020). Protein purity was
560 confirmed by SDS-PAGE using 4–20% Mini-PROTEAN TGX protein Gels (BioRad).
561
562 **Transient DNA Transfection**
563 HeLa cells were plated at on 18 mm glass coverslips at a concentration of ≈5×10^4
564 cells.mL^{-1}, 16-24 hr prior to transfection. FuGENE 6 (Promega) transfection reagent was used
565 according to the manufacturer's instructions to transfect HeLa cells at a 3:1 ratio (using 1.5 µL
566 FuGENE 6 and 0.5 µg DNA per well). RAW264.7 cells were plated on 18 mm glass coverslips
567 at ≈2×10^5 cells.mL^{-1}, 16-24 hr prior to transfection. FuGENE HD (Promega) transfection reagent
568 was used to transfect RAW264.7 cells at a 3.5:1 ratio (using 1.75 µL FuGENE HD and 0.5 µg
569 DNA per well). In all cases, monolayers were used for experiments 16 hr after transfection.
570
571 **Ratiometric fluorescence microscopy for the measurement of lysosomal pH, V-ATPase**
572 **activity and buffering power**
573 HeLa cells were plated on 18 mm glass coverslips and incubated overnight with 250 µg.mL^{-1}
574 fluorescein isothiocyanate (FITC)-conjugated 10 kDa-dextran, which was then chased for 1 h in
575 complete medium prior to imaging to visualize lysosomes. Coverslips were then mounted in a
576 Chamlide magnetic chamber and incubated in HBSS medium for fluorescence-based pH
577 determinations.
578 Steady-state lysosomal pH was determined by exciting FITC-dextran labelled lysosomes
579 sequentially at 481±15 nm and 436± 20 nm, collecting emitted light at 520±35 nm. The

fluorescence intensity of FITC when excited at ≈490 nm is highly pH dependent and was used to determine the pH of lysosomes. The fluorescence when excited at ≈440 nm is much less pH dependent and was used to correct for potential photobleaching or focal changes during image acquisition, the 490 nm/440 nm fluorescence ratio of FITC is utilized to determine pH values. Multiple fields of cells were imaged, and the data processed with Volocity.

The 490 nm/440 nm fluorescence ratios were converted to pH by sequentially incubating the cells for 5 min in isotonic K^+ solutions (143 mM KCl, 5 mM glucose, 1 mM $MgCl_2$, 1 mM $CaCl_2$) of different pH (pH 4.5, buffered with 20 mM acetic acid, pH 5.5, 6.5, 7.5 solutions buffered with 20 mM MES), containing 10 µM nigericin and 5 µM monensin. Background-subtracted 490/440 nm fluorescence ratios were then plotted against pH, and the data fitted by least squares were used to interpolate the lysosomal pH.

For V-ATPase activity determinations, HeLa cells were acutely treated with 500 nM concanamycin A and images were acquired at 30 s intervals for 10 min. The time dependence of the resulting pH changes was then plotted in GraphPad Prism 6, and the initial rates of alkalinization (per cell) were determined within 2 min of addition of concanamycin A.

For the determination of buffering power, HeLa cells containing FITC-dextran loaded lysosomes were challenged with 0.5 mM NH_4Cl and the resulting change in fluorescence intensity (490 nm/440 nm) was measured immediately. The corresponding pH change, calculated as above, was used to calculate the concentration of NH_4^+ formed inside the lysosome, using the Henderson-Hasselbalch equation, and the buffering capacity estimated as $\Delta[NH_4^+]_{lys}/\Delta pH_{lys}$.

Lysosome labeling, cresyl violet staining and dissipation of organellar pH

For identification of lysosomes, HeLa cells were incubated overnight with 100 µg.mL^{-1} fluorescently-conjugated 10 kDa-dextran at the time of transient transfection, 16 to 24 hr prior to

experiments. The next day, monolayers were washed 3× with PBS and placed in HBSS medium at 37ºC for 1 hr to chase the dextran to lysosomes. Monolayers were then imaged live by confocal microscopy.

For cresyl violet staining, HeLa cells, seeded on 18 mm glass coverslips at a concentration of 1×10^5 cells.mL^{-1}, were labeled with fluorescent dextran as described above. Monolayers were then incubated at 37ºC with 1 μM cresyl violet in Hanks' Balanced Salt Solution (HBSS; MultiCell, Wisent) for 5 min, washed 3 times and imaged live by confocal microscopy. In some cases, organellar pH was dissipated prior to cresyl violet staining. To this end the cells were treated for 30 min with 250 nM concanamycin A and 10 mM NH_4Cl in HBSS. After this treatment, monolayers were stained with 1 μM cresyl violet and imaged live, as above.

Fluorescent labeling of SidK$_{1\text{-}278}$

Prior to labeling, purified SidK$_{1\text{-}278}$-3×FLAG (see above; referred to in the text as SidK) was buffer exchanged into PBS using a centrifugal concentrator (EMD Millipore). Following this, SidK was directly labeled by conjugation with Alexa Fluor-568 NHS-ester (Invitrogen). A 10:1 dye:SidK molar ratio was prepared in 0.05 M borate buffer, vortexed, and incubated shaking at 500 rpm for 1 hr at room temperature. Labeled SidK (referred to as SidK-AL568) was then dialyzed in 4× 1 L PBS, to remove unincorporated dye. One volume of 100% glycerol was added to the SidK-AL568 for stability, and stored at 4°C.

The fraction of SidK labeled with Alexa Fluor-568 was determined using absorbance spectroscopy on a Nanodrop 2000 instrument (Thermo Scientific). SidK and SidK-AL568 was diluted to 0.1 mg.mL^{-1} in PBS. The *A*280 of SidK and its molecular weight (34,646 g.mol^{-1}) was used to calculate its extinction coefficient (ε *SidK* = 41,690 cm^{-1}.M^{-1}). Then, the *A*280 and *A*577 (λ_{max} of Alexa Fluor 568) of SidK-AL568 were measured and the degree of labeling (moles of dye per mole of protein) for SidK-AL568 calculated, using the following two equations, along

with the ε *dye* value for Alexa Fluor 568 (91,300 $cm^{-1}.M^{-1}$) and the correction factor for the *A*280 contribution of Alexa Fluor-568 (*CF*280 = 0.46):

$$(1)\quad \text{protein concentration (M)} = \frac{[A280-(A577 \times CF280)] \times \text{dilution factor}}{\varepsilon\ SidK}$$

$$(2)\quad \text{moles dye per mole protein} = \frac{A577 \times \text{dilution factor}}{\varepsilon\ dye \times \text{protein concentration}}$$

The number of dye particles per SidK-AL568 molecule was determined by single-molecule photobleaching imaging (Liesche et al., 2015). Briefly, a 10^6 dilution of SidK-AL568 was prepared and added to clean coverslips, creating a monodispersed sample. Monodispersed SidK-AL568 was then imaged continuously by confocal microscopy at ≈ 5 $frames.sec^{-1}$, until spot disappearance occurred through photobleaching. Time series images were analyzed using Volocity v6.3 software (Quorum Technologies), and SidK-AL568 molecule fluorescence over time plotted to generate traces where the number of steps required for SidK-AL568 spot disappearance were counted. Each step corresponded to a single Alexa 568 dye molecule conjugated to SidK. The average fluorescence value for *bona fide* single bleach step SidK-AL568 was used to calculate the percent of SidK-AL568 in the monodispersed population with 1, 2, 3, or 4 or 5+ dye molecules per SidK.

Culturing of yeast and immunofluorescence of yeast spheroplasts

Wild type (*MATα ura3–52 leu2–3,112 his4–519 ade6)* and *vma1Δ (MATα ura3–52 leu2–3,112 his4–519 ade6 vma1Δ::LEU2*) *S. cerevisiae* strains were kindly gifted by Dr. Morris Manolson (University of Toronto). Yeast cultures were routinely grown at 30°C, with shaking, in YPD medium (BD Biosciences).

For spheroplast preparation, overnight cultures were diluted 1:100 in YPD broth and grown at 30°C for 2 hr. One mL of yeast culture was then fixed with 4% PFA for 30 min, while shaking at room temperature. After washing cells 2× with 0.1 M $KHPO_4$ pH 6.5, yeast were

washed 1× in K-Sorb (1.2 M sorbitol in 0.1 M $KPHO_4$) and resuspended in 0.5 mL K-Sorb containing 5 µL β-mercaptoethanol and 10 $mg.mL^{-1}$ zymolyase 20T (MP Biomedicals). Cells were shaken at room temperature for 30 min, and gently washed 2× with K-Sorb. After final resuspension in 0.5 mL K-Sorb, 20 µL of spheroplast suspension was spread on a concanavalin A-coated slide and allowed to adhere for 15 min at room temperature. Following this, spheroplasts were permeabilized/blocked for 30 min in PBS 0.1% Tween-20 containing 5% BSA and 5% skim milk. Samples were then incubated in the same buffer containing 1:200 SidK-AL568 and 1 $µg.mL^{-1}$ DAPI for 30 min at room temperature. After staining, slides were washed 3× with PBS and visualized by confocal microscopy.

Immunofluorescence of mammalian cells

After fixing in 3% PFA for 10 min at room temperature, cells were washed in PBS and permeabilized/blocked in PBS containing 5% BSA and 0.1% Triton X-100 for 30 min at room temperature. Samples were then incubated with primary staining reagents for 30 min at room temperature. Primary antibody dilutions were: LAMP1 (1:50), VapB (1:100), TGN46 (1:100), GM130 (1:100), V1A (1:100). For mitochondrial staining, fluorescently-conjugated streptavidin was used at 1:100 dilution. SidK-AL568 was used at 1:100, 1:50 or 1:25 dilution, as indicated in the text. Where indicated, a 5-fold excess of unlabeled $SidK_{1-278}$ was used in the blocking/permeabilization step, to block SidK-AL568 binding sites prior to the addition of SidK-AL568. After primary staining, monolayers were washed 3× with PBS, and samples incubated 30 min at room temperature with Alexa Fluor-conjugated secondary antibodies at a 1:1000 dilution. Where indicated, 1:1000 fluorescent phalloidin or $1µg.mL^{-1}$ DAPI was added together with the secondary antibodies. Samples were washed 3× with PBS and viewed by confocal microscopy in PBS.

Phagosome and sucrosome analyses

For phagocytosis assays, RAW264.7 cells were plated at on 18 mm glass coverslips at a concentration of 2×10^5 cells.mL^{-1} and grown for 16-24 hr. Cells were transfected as described above with the constructs indicated in the text. The day of experiments, SRBCs were prepared for use in phagocytosis. Briefly, 100 µL of SRBC suspension was washed with 3× with PBS and labeled with Alexa Fluor-405 NHS ester for 20 min, shaking at room temperature. SRBC were then opsonized with 2 µL of rabbit anti-SRBC IgG at 37°C for 1 h. Prepared SRBCs were washed 3× with PBS and resuspended to a final volume of 1 mL in PBS. After 1:10 dilution in PBS, 25 µL of this suspension was added to the RAW264.7 cells. Alternatively, FITC-labelled zymosan was diluted to 10 mg.mL^{-1} in PBS and opsonized by incubation with human IgG (final IgG concentration, 5 mg.mL^{-1}) for 30 min at room temperature. Prepared zymosan was then washed 3× with PBS and resuspended to a final volume of 20 µL in PBS. 1 µL of this suspension was added to RAW264.7 seeded onto coverslips. In all cases, phagocytosis was synchronized by sedimenting particles onto the cells using centrifugation at 300 ×*g* for 1 min. After phagocytosis, monolayers were fixed in 3% PFA for 10 min at room temperature and stored in PBS until used. FITC-zymosan phagocytosis, which was used to determine the rate of acidification of the nascent phagosome, was imaged immediately after sedimentation of the particles.

To generate sucrosomes, transfected RAW264.7 cells were incubated for 16 to 24 hr in RPMI-1640 medium containing L-glutamine, 10% heat-inactivated FCS and 30 mM sucrose, at 37°C under 5% CO_2. The next day, cells were washed 3× with PBS, placed in RPMI-1640 medium containing L-glutamine and 10% heat-inactivated FCS, and used for experiments as described in the text. After experiments, monolayers were fixed in 3% PFA for 10 min at room temperature and stored in PBS.

Quantitation of the number of SidK-AL568 per lysosome

The average fluorescence value of monodispersed SidK-AL568 molecules was used to

estimate the number of SidK-AL568 monomers per lysosome in HeLa cells that had been co-stained with SidK-AL568 and LAMP1. 1:25, 1:50 and 1:100 SidK-AL568 dilutions were assessed to determine the conditions required for saturation of SidK-AL568 staining, needed to estimate the maximum number of SidK-AL568 molecules bound per $LAMP1^+$ lysosome.

Microscopy

Confocal images were acquired using a spinning disk system (Quorum Technologies Inc.). The instrument consists of a microscope (Axiovert 200M; Zeiss), scanning unit (CSU10; Yokogawa Electric Corporation), electron-multiplied charge-coupled device camera (C9100-13; Hamamatsu Photonics), five-line (405-, 443-, 491-, 561-, and 655-nm) laser module (Spectral Applied Research), and filter wheel (MAC5000; Ludl) and is operated by Volocity v6.3. Images were acquired using a 63×/1.4 NA oil objective (Zeiss), with an additional 1.5× magnifying lens and the appropriate emission filter. For live experiments, cells were maintained at 37°C using an environmental chamber (Live Cell Instruments).

Ratiometric fluorescence pH measurements were acquired on an epifluorescence microscope (Axiovert 200M; Zeiss) running on Volocity v6.3, equipped with a camera (Flash 4.0v2; Hamamatsu), excitation lamp (X-Cite 120; EXFO Life Sciences Group), a 63x/1.4 NA oil objective (Zeiss), the appropriate dichroic mirror (CFP/YFP; Chroma Technology), and filter wheels containing the necessary filters for FITC ratiometric fluorescence determinations (excitation at 481±15 nm or 436±20 nm, emission 520±35 nm). All experiments were performed maintaining the temperature at 37^oC with an environmental controller (Medical Systems Corporation).

Image analysis

Image processing and analyses were performed using Volocity v6.3. Image

deconvolution was done on acquired Z-stacks within the Volocity Restoration module, using the iterative restoration function. Calculated fluorochrome point spread functions were used to deconvolve individual channels for 5-8 iterations, until a confidence limit of >90% was achieved. For colocalization analyses, Volocity Colocalization module was used to calculate the positive product of the differences of the mean channels (Li, 2004), which was then overlaid on merged images for visualization. Alternatively, for some colocalization analyses, Manders' overlap coefficients were calculated in Volocity, which describe the percent of various organelle markers that colocalize with SidK-AL568 (referred to as M).

The Volocity Ratio function was used for SidK-AL568 ratio calculations. This divides background-subtracted intensities of SidK-AL568 and lysosomal, sucrosomal or phagosomal markers (as indicated in the text), to calculate the ratio of SidK-AL568 fluorescence to that of the chosen organellar marker. The Ratio function generates a rainbow LUT ratio channel that is applied as an overlay on merged images, with a scale representing ratio values from 0 to 2.

General methodology and statistics

Data calculations and normalizations were done using Microsoft Excel 2011 (Microsoft Corporation) or GraphPad Prism v9 software (GraphPad Software, Inc.). Because experiments were, for the most part, *in vitro* imaging determinations of individual cells, samples were assigned to groups according to specific experimental treatments (control vs. experimental group). The number of individual experiments and the number of determinations per experiment were selected to attain an estimate of the variance compatible with the statistical tests used, primarily student's *t* test. Each type of experiment was performed a minimum of three separate times (biological replicates) and a minimum of ten individual event determinations (equivalent, but not identical to technical replicates). Data was tested for normality, and appropriate testing applied. No data was excluded as outliers. All statistics were calculated using GraphPad Prism v9.

Data availability

Experimental datasets that support the findings of this study are available from the corresponding authors upon reasonable request.

Online supplemental material

Figure S1 shows the (**A**) SidK-AL568 or (**B**) α-V1A staining of HeLa cells before (left) and after (right) the thresholding used in the colocalization analyses (Costes et al., 2004) of Figure 4**C** and 4**H**, respectively.

FIGURE LEGENDS

Figure 1. SidK interacts with the V-ATPase *in vitro* and when expressed in mammalian cells. A. SDS-PAGE of 3×FLAG $SidK_{1-278}$ to illustrate purity of the probe and its ability to allow isolation of yeast V-ATPase by affinity chromatography. Bands corresponding to $SidK_{1-278}$ and to individual subunits of V-ATPase are labeled. **B.** Model of the yeast V-ATPase with $SidK_{1-278}$-GFP bound, generated from PDB accession numbers 5VOX, 1GFL, and 6O7T. **C.** Visualization of $SidK_{high}$ cells. Lysosomes of HeLa cells were transfected with SidK-GFP (green) and loaded with Alexa Fluor-647-labelled 10 kDa dextran (magenta). Side panels show the individual SidK and 10 kDa dextran channels in the region denoted by the dotted square, at 2.2× magnification. **D.** Visualization of $SidK_{low}$ cells (green) labeled for lysosomes as in **C**. Side panels show the individual SidK and 10 kDa dextran channels denoted by the dotted square, at 2.0× magnification. **E** and **F.** Lysosomes were identified by LAMP1 immunostain (magenta) after expression of high levels of SidK-GFP ($SidK_{high}$; green). Prior to fixation and immunostaining, cells were either left untreated (**E**) or permeabilized with pneumolysin (PLY) to remove excess cytosolic SidK-GFP (**F**). Side panels show the individual SidK and LAMP1 channels. Here and elsewhere, outlines of cells are indicated by dotted lines when required. Images in **C-F** are extended focus compressions of confocal images representative of ≥ 30 fields from ≥ 3 separate experiments of each type. All scale bars: 5 μm.

Figure 2. Effect of SidK-fluorescent protein overexpression on the pH of acidic compartments. A. Localization of endogenous LAMP1 (green) in untreated control cells. **B.** Localization of LAMP1 (green) in cells expressing SidK-mCherry (red). Side panels show the individual SidK and LAMP1 channels in the area denoted by the dotted square, at 2.0× magnification. Arrowheads mark sites of peripheral LAMP1 accumulation. **C.** Localization of LAMP1 (green) in cells treated with 250 nM concanamycin A for 1 hr. Arrowheads mark sites of peripheral LAMP1 accumulation. **D.** Retention of the acidotropic dye cresyl violet (magenta) in

cells expressing SidK-GFP (green), where lysosomes had been preloaded with Alexa Fluor-647-conjugated 10 kDa dextran (blue). Side panels show the individual channels of the area denoted by the dotted square, at 2.7× magnification. **E.** Cells expressing SidK-GFP (green) and labeled for lysosomes (blue) were treated with 250 nM concanamycin A and 10 mM NH_4Cl for 30 min to neutralize luminal pH. After treatment, cells were incubated with cresyl violet as in **D**. Side panels are 2.7× magnification. Images in **A-E** are extended focus images representative of ≥ 30 fields from ≥ 3 separate experiments of each type. All scale bars: 5 μm. **F.** Lysosomal pH was determined in $SidK^-$ and $SidK^+$ HeLa cells. The lysosomes of control or SidK-mCherry-transfected HeLa cells were loaded overnight with FITC-10 kDa dextran. Lysosomal pH was subsequently measured by ratiometric fluorescence microscopy as described in the Materials and Methods. For each condition, 3 independent experiments were quantified, with ≥ 20 cells per replicate. Data are means ± SEM. *p* value was calculated using unpaired, 2-tailed student's t-test. **G.** Lysosomal V-ATPase activity was measured in control and SidK-mCherry-expressing HeLa cells acutely treated with 500 nM concanamycin A. V-ATPase activity was determined from the inverse rate of alkalization upon the addition of concanamycin A. See Materials and Methods for further details. For each condition, three independent experiments were quantified, with ≥ 10 cells per replicate. Data are means ± SEM. *p* value was calculated using unpaired, 2-tailed student's t-test.

Figure 3. SidK-AL568 specifically labels the V-ATPase. A. HeLa cells were stained with SidK-AL568 (red) as described in the Materials and Methods either directly (left) or after incubation with a 5-fold excess of unlabeled $SidK_{1-278}$ (right). F-actin was labeled with fluorescent phalloidin (blue). **B.** Spheroplasts of wild type or *vma1*Δ *S. cerevisiae* were prepared and stained with SidK-AL568 (red) as detailed in Materials and Methods. Nuclei were labeled with DAPI (cyan). Outlines of the spheroplasts, visualized by DIC, are indicated by dotted lines. **C** and **D.** HeLa cells were transfected with V_Oa2- (**C**) or V_Oa3-GFP (**D**) constructs (green), and

819 stained using SidK-AL568 (magenta). Nuclei were labeled with DAPI (blue). Outlines of cells are
820 indicated by dotted lines. Side panels show the individual SidK-AL568 and V_Oa channels.
821 Colocalization between SidK-AL568 and the corresponding V_Oa subunit is shown in orange and
822 the calculated Manders' coefficient (M) between the a subunit and SidK-AL568 is indicated. **A-D**
823 are extended focus compressions of confocal images representative of ≥ 30 fields from ≥ 3
824 separate experiments of each type. All scale bars: 5 µm.
825
826 **Figure 4. Localization of the V-ATPase in mammalian cells using SidK-AL568.**
827 **A**. HeLa cells were stained with SidK-AL568 (red), as described in Materials and Methods.
828 Nuclei were labeled with DAPI (blue). Arrowheads mark peripheral, likely endocytic, vesicles
829 (open) and juxtanuclear vesicles and cisternae, likely including the Golgi compartment (closed).
830 **B-F.** V-ATPase in HeLa cells was labeled with SidK-AL568 (magenta) and co-stained for **B**:
831 LAMP1, **C:** *trans*-Golgi, **D:** *cis*-Golgi, **E:** ER, and **F:** mitochondria (green) as described in the
832 text. Nuclei were labeled with DAPI (blue). Side panels show the individual SidK-AL568 and
833 organelle channels in the area denoted by the dashed square, at 1.1, 0.9, 1.1, 1.7 and 1.5×
834 magnification, respectively. Outlines of cells are indicated by dotted lines. **G** and **H.** HeLa cells
835 were immunostained using a commercially available V_1A antibody (Abnova; catalogue no.
836 H00000523-M02; shown in magenta) in cells co-stained for LAMP1 (**G**) or *trans*-Golgi (**H**), in
837 green. Nuclei were labeled with DAPI (blue). Side panels show the individual α-V_1A and
838 organelle channels marked by the dotted square, at 1.1 and 1.4× magnification, respectively. **A-**
839 **H** are extended focus images representative of ≥ 30 fields from ≥ 3 separate experiments of
840 each type. Outlines of cells are indicated by dotted lines. Colocalization and Manders'
841 coefficients (M) between the organellar marker and V-ATPase probe are shown in orange. All
842 scale bars: 5 µm.
843

Figure 5. The acidification of macrophage phagosomes parallels the recruitment of the V-ATPase to the phagosomal membrane, as detected by SidK-AL568. A. RAW264.7 cells were incubated with IgG-opsonized FITC-zymosan, which were sedimented by centrifugation onto the coverslip to initiate phagocytosis. Phagosomal pH changes were determined by ratiometric fluorescence microscopy, as described in the Materials and Methods. Time 0 marks the point where phagosome acidification became evident. Data points (open circles) represent the average of 2 independent experiments, with ≥ 10 cells per replicate. **B.** Schematic showing the stages of phagosome engulfment and maturation, with associated membrane markers. **C.**V-ATPase localization in resting RAW264.7 cells stained with SidK-AL568 (magenta). **D-H**. RAW264.7 cells that had been transfected with the indicated phagosomal maturation markers (green) were allowed to internalize IgG-opsonized SRBCs for various times before fixation. The cells were then fixed, permeabilized, and stained with SidK-AL568 (magenta). **D.** Cells expressing a plasma membrane (PM) marker, fixed 2 min after initiation of phagocytosis. **E.** Cells expressing Rab5A, fixed 5 min after initiation of phagocytosis. **F.** Cells expressing a PtdIns(3)P-specific probe, fixed 5 min after initiation of phagocytosis. **G.** Cells expressing Rab7 marker, fixed 30 min after initiation of phagocytosis. **H.** Cells immunostained for LAMP1, fixed 30 min after initiation of phagocytosis. **C-H** Are *XY* optical slices acquired near the middle of the cell or phagosome, representative of ≥ 30 fields from ≥ 3 separate experiments of each type. Outlines of cells are indicated by dotted lines. All scale bars: 5 μm.

Figure 6. V-ATPase accumulates in subdomains along the phagosomal membrane and is excluded from ER contact sites. A. RAW264.7 cells that had been transfected with ORP1L-GFP were allowed to internalize IgG-opsonized SRBCs and fixed after 60 min. Cells were stained with SidK-AL568 (magenta) and visualized along with ORP1L (cyan). Individual SidK-AL568 and ORP1L channels and the SidK-AL568:ORP1L fluorescence ratio ($Ratio_{SidK\text{-}AL568:ORP1L}$) are shown from left to right. Fluorescence ratio is pseudocolored in a rainbow LUT,

corresponding to ratio values from 0 to 2. **B.** RAW264.7 cells that had been transfected with Arl8b-GFP were allowed to internalize IgG-opsonized SRBCs and fixed after 30 min. Cells were stained with SidK-AL568 (magenta) and visualized along with Arl8b-GFP (cyan). Individual channels and the pseudocolored fluorescence ratio are shown from left to right. **C.** Human M0 macrophages were allowed to internalize IgG-opsonized SRBCs and fixed after 30 min. Cells were fixed, permeabilized and stained with SidK-AL568 (magenta) and immunostained for endogenous VapB (cyan). Smaller panels show individual SidK-AL568, VapB and SidK-AL568:VapB fluorescence ratio channels ($Ratio_{SidK\text{-}AL568:VapB}$) (top to bottom) for 3 individual phagosomes (left to right) identified by the dotted squares, all at 1.8× magnification. **A-C** are central *XY* optical slices optical slices acquired near the middle of the cell or phagosome representative of ≥ 30 fields from ≥ 3 separate experiments of each type. Outlines of cells are indicated by dotted lines. All scale bars: 5 μm.

Figure 7. Lysosomes and lysosomal tubules in a variety of cell types show V-ATPase subdomains. A. RAW264.7 cells transfected with ORP1L-GFP were subjected to lysosome enlargement by overnight treatment with 30 mM sucrose, as described in the Materials and Methods. Cells were stained with SidK-AL568 (magenta) and the distribution of V-ATPase in sucrosomes labeled with ORP1L (cyan) visualized. Side panels show the individual SidK-AL568, ORP1L and colocalization channels (left to right). Colocalization and Manders' coefficient between ORP1L and SidK-AL568 (M) are shown in orange. **B.** RAW264.7 cells transfected with Arl8b-GFP were subjected to lysosome enlargement by overnight treatment with 30 mM sucrose. Cells were stained with SidK-AL568 (magenta) and the distribution of V-ATPase in sucrosomes labeled with Arl8b (cyan) visualized. Side panels show the individual SidK-AL568, Arl8b and colocalization channels (left to right). Colocalization and Manders' coefficients between Arl8b and SidK-AL568 (M) are shown in orange. **C-E** Localization of the V-ATPase in tubular lysosomal structures in: **C.** RAW264.7 cells, **D.** human M0 macrophages, and

E. HeLa cells. Cells were stained using SidK-AL568 (magenta) and immunostained for endogenous LAMP1 (cyan). Solid white arrowheads mark lysosomal regions that are $SidK^+$ $LAMP1^-$, while open arrowheads mark regions that are $SidK^-$ $LAMP1^+$. Side panels show individual SidK-AL568, LAMP1 and colocalization channels (top to bottom). Colocalization and Manders' coefficients between LAMP1 and SidK-AL568 (M) are shown in orange. **A-E** are *XY* optical slices representative of ≥ 30 fields from ≥ 3 separate experiments of each type. All scale bars: 5 µm.

Figure 8. Estimation of the number of V-ATPases per lysosomal compartment. A. Photobleaching of monodisperse SidK-AL568. Representative intensity-time traces for a single SidK-AL568 labeled with 1 (top) or 2 (bottom) Alexa Fluor 568 moieties. Loss of fluorescence after complete photobleaching is shown by the dotted red lines. **B.** Histogram showing the measured number of dye molecules per SidK-AL568 monomer determined analyzing > 5000 single molecule photobleaching traces. The number of SidK-AL568 molecules in each category of the histogram is indicated above the bar. **C.** HeLa cells were stained with SidK-AL568 at varying concentrations (shown in absolute concentration and as dilution). Lysosomal fluorescence was plotted to determine the concentration of SidK-AL568 required to reach maximal lysosome fluorescence, indicative of saturation of available binding sites. **D.** HeLa cells were stained with SidK-AL568 using the near-saturation conditions determined in **C** (1:50). Total fluorescence per lysosome was compared to the average fluorescence of a single molecule of SidK-AL568 and is displayed; the average number of SidK-AL568 molecules bound per lysosome is indicated by the horizontal line, as is the SE (whiskers). A total of 5715 lysosomes from 2 independent experiments were quantified. **E.** Intracellular V-ATPase distribution among lysosomes is heterogeneous. HeLa cells were stained with SidK-AL568 (magenta) using the near-saturating conditions determined in **C** (1:50), and co-stained for LAMP1 (green). Side panels show the individual LAMP1 (top), and SidK-AL568:LAMP1 colocalization channels

(bottom) for juxtanuclear (left) or peripheral (right) lysosomes in the areas denoted by the dotted squares. Outlines of cells and lysosomes are indicated by dotted or solid lines, respectively. **F.** SidK-AL568:LAMP1 fluorescence ratio ($Ratio_{SidK\text{-}AL568:LAMP1}$) corresponding to image in **E**. The fluorescence ratio was pseudocolored in a rainbow LUT, representing ratio values from 0-2. **G.** Shell analysis of SidK distribution as a function of distance from the cell outer edge. HeLa cells were stained using SidK-AL568 and co-stained for LAMP1. Cell outlines were drawn and degraded iteratively inward by 4 µm to create concentric shells (colored differentially) within each cell that were used to subgroup LAMP1+ lysosomes for subsequent analysis. **H.** For each shell, total fluorescence per lysosome was compared to the average fluorescence of a single molecule of SidK-AL568, and the average number of SidK-AL568 molecules bound per lysosome calculated, as a function of distance from the cell outer edge. Data are means ± SEM of 2 independent experiments with ≥ 5 cells per replicate. *N* = 791, 1112, 1203, 1275 and 1334 lysosomes analyzed for shells 0-4, 4-8, 8-12, 12-16, and >16 µm from the cell edge, respectively. Images in **E-G** are extended focus compressions of confocal images representative of ≥ 10 fields from ≥ 2 separate experiments of each type. All scale bars: 5 µm.

SUPPLEMENTAL FIGURE LEGEND

Figure S1. Demonstration of the Costes thresholding method used prior to colocalization analyses. HeLa cells were stained with (**A**) SidK-AL568 (magenta) or (**B**) α-V_1A (magenta), as described in Materials and Methods. For both **A** and **B**, left panel shows staining before Costes thresholding, while the right panel shows the same channel after thresholding. Outlines of cells are indicated by dotted lines. Scale bars: 5 µm. Images in **A** and **B** correspond to Figure 4C and 4H, respectively.

946 REFERENCES
947
948 Abbas, Y.M., D. Wu, S.A. Bueler, C.V. Robinson, and J.L. Rubinstein. 2020. Structure of V-
949 ATPase from the mammalian brain. *Science*. 367:1240–1246. doi:10.1126/science.aaz2924.

950 Alzamora, R., R.F. Thali, F. Gong, C. Smolak, H. Li, C.J. Baty, C.A. Bertrand, Y. Auchli, R.A.
951 Brunisholz, D. Neumann, K.R. Hallows, and N.M. Pastor-Soler. 2010. PKA Regulates
952 Vacuolar H+-ATPase Localization and Activity via Direct Phosphorylation of the A Subunit in
953 Kidney Cells. *Journal of Biological Chemistry*. 285:24676–24685.
954 doi:10.1074/jbc.M110.106278.

955 de Araujo, M.E.G., G. Liebscher, M.W. Hess, and L.A. Huber. 2020. Lysosomal size matters.
956 *Traffic (Copenhagen, Denmark)*. 21:60–75. doi:10.1111/tra.12714.

957 Balgi, A.D., G.H. Diering, E. Donohue, K.K.Y. Lam, B.D. Fonseca, C. Zimmerman, M. Numata,
958 and M. Roberge. 2011. Regulation of mTORC1 signaling by pH. *PLoS One*. 6:e21549.
959 doi:10.1371/journal.pone.0021549.

960 Banerjee, S., K. Clapp, M. Tarsio, and P.M. Kane. 2019. Interaction of the late endo-lysosomal
961 lipid PI(3,5)P2 with the Vph1 isoform of yeast V-ATPase increases its activity and cellular
962 stress tolerance. *The Journal of biological chemistry*. 294:jbc.RA119.008552-9171.
963 doi:10.1074/jbc.RA119.008552.

964 Bright, N.A., L.J. Davis, and J.P. Luzio. 2016. Endolysosomes Are the Principal Intracellular
965 Sites of Acid Hydrolase Activity. *Current biology : CB*. 26:2233–2245.
966 doi:10.1016/j.cub.2016.06.046.

967 Bright, N.A., B.J. Reaves, B.M. Mullock, and J.P. Luzio. 1997. Dense core lysosomes can fuse
968 with late endosomes and are re-formed from the resultant hybrid organelles. *Journal of cell*
969 *science*. 110 (Pt 17):2027–2040.

970 Bucci, C., P. Thomsen, P. Nicoziani, J. McCarthy, and B. van Deurs. 2000. Rab7: a key to
971 lysosome biogenesis. *Mol Biol Cell*. 11:467–480. doi:10.1091/mbc.11.2.467.

972 Butor, C., G. Griffiths, N.N. Aronson, and A. Varki. 1995. Co-localization of hydrolytic enzymes
973 with widely disparate pH optima: implications for the regulation of lysosomal pH. *J Cell Sci*.
974 108 (Pt 6):2213–2219.

975 Capecci, J., and M. Forgac. 2013. The Function of Vacuolar ATPase (V-ATPase) a Subunit
976 Isoforms in Invasiveness of MCF10a and MCF10CA1a Human Breast Cancer Cells. *Journal*
977 *of Biological Chemistry*. 288:32731–32741. doi:10.1074/jbc.M113.503771.

978 Casey, J.R., S. Grinstein, and J. Orlowski. 2009. Sensors and regulators of intracellular pH.
979 *Nature Reviews Molecular Cell Biology*. 11:50–61.

980 Castroflorio, E., J. den Hoed, D. Svistunova, M.J. Finelli, A. Cebrian-Serrano, S. Corrochano,
981 A.R. Bassett, B. Davies, and P.L. Oliver. 2021. The Ncoa7 locus regulates V-ATPase
982 formation and function, neurodevelopment and behaviour. *Cell. Mol. Life Sci.* 78:3503–3524.
983 doi:10.1007/s00018-020-03721-6.

984 Chen, Y., B. Wu, L. Xu, H. Li, J. Xia, W. Yin, Z. Li, D. Shi, S. Li, S. Lin, X. Shu, and D. Pei. 2012.
985 A SNX10/V-ATPase pathway regulates ciliogenesis in vitro and in vivo. *Cell Res*. 22:333–
986 345. doi:10.1038/cr.2011.134.

987 Cheng, X.-T., Y.-X. Xie, B. Zhou, N. Huang, T. Farfel-Becker, and Z.-H. Sheng. 2018.
988 Characterization of LAMP1-labeled nondegradative lysosomal and endocytic compartments
989 in neurons. *Journal of Cell Biology*. 217:3127–3139. doi:10.1083/jcb.201711083.

990 Clarke, M., L. Maddera, U. Engel, and G. Gerisch. 2010. Retrieval of the Vacuolar H+-ATPase
991 from Phagosomes Revealed by Live Cell Imaging. *PLoS ONE*. 5:e8585.
992 doi:10.1371/journal.pone.0008585.

993 Cohn, Z.A., and B.A. Ehrenreich. 1969. The uptake, storage, and intracellular hydrolysis of
994 carbohydrates by macrophages. *The Journal of experimental medicine*. 129:201–225.

995 Colacurcio, D.J., and R.A. Nixon. 2016. Disorders of lysosomal acidification—The emerging role
996 of v-ATPase in aging and neurodegenerative disease. *Ageing Research Reviews*. 32:75–88.
997 doi:10.1016/j.arr.2016.05.004.

998 Costes, S.V., D. Daelemans, E.H. Cho, Z. Dobbin, G. Pavlakis, and S. Lockett. 2004. Automatic
999 and quantitative measurement of protein-protein colocalization in live cells. *Biophys J*.
1000 86:3993–4003. doi:10.1529/biophysj.103.038422.

1001 DeCourcy, K., and B. Storrie. 1991. Osmotic swelling of endocytic compartments induced by
1002 internalized sucrose is restricted to mature lysosomes in cultured mammalian cells.
1003 *Experimental cell research*. 192:52–60.

1004 Eaton, A.F., M. Merkulova, and D. Brown. 2021. The H+-ATPase (V-ATPase): from proton
1005 pump to signaling complex in health and disease. *American Journal of Physiology-Cell*
1006 *Physiology*. 320:C392–C414. doi:10.1152/ajpcell.00442.2020.

1007 Ferris, A.L., J.C. Brown, R.D. Park, and B. Storrie. 1987. Chinese hamster ovary cell lysosomes
1008 rapidly exchange contents. *J Cell Biol*. 105:2703–2712. doi:10.1083/jcb.105.6.2703.

1009 Fisher, J.M., and R.H. Scheller. 1988. Prohormone processing and the secretory pathway. *J*
1010 *Biol Chem*. 263:16515–16518.

1011 Futai, M., G.-H. Sun-Wada, Y. Wada, N. Matsumoto, and M. Nakanishi-Matsui. 2019. Vacuolar-
1012 type ATPase: A proton pump to lysosomal trafficking. *Proceedings of the Japan Academy.*
1013 *Series B, Physical and biological sciences*. 95:261–277. doi:10.2183/pjab.95.018.

1014 Goddard, T.D., C.C. Huang, E.C. Meng, E.F. Pettersen, G.S. Couch, J.H. Morris, and T.E.
1015 Ferrin. 2018. UCSF ChimeraX: Meeting modern challenges in visualization and analysis.
1016 *Protein Sci*. 27:14–25. doi:10.1002/pro.3235.

1017 Hosokawa, H., P.V. Dip, M. Merkulova, A. Bakulina, Z. Zhuang, A. Khatri, X. Jian, S.M. Keating,
1018 S.A. Bueler, J.L. Rubinstein, P.A. Randazzo, D.A. Ausiello, G. Grüber, and V. Marshansky.
1019 2013. The N termini of a-subunit isoforms are involved in signaling between vacuolar H+-
1020 ATPase (V-ATPase) and cytohesin-2. *The Journal of biological chemistry*. 288:5896–5913.
1021 doi:10.1074/jbc.M112.409169.

1022 Hu, Y., L.R. Carraro-Lacroix, A. Wang, C. Owen, E. Bajenova, P.N. Corey, J.H. Brumell, and I.
1023 Voronov. 2016. Lysosomal pH Plays a Key Role in Regulation of mTOR Activity in
1024 Osteoclasts. *J Cell Biochem*. 117:413–425. doi:10.1002/jcb.25287.

1025 Huotari, J., and A. Helenius. 2011. Endosome maturation. *The EMBO Journal*. 30:3481–3500.
1026 doi:10.1038/emboj.2011.286.

1027 Hurtado-Lorenzo, A., M. Skinner, J.E. Annan, M. Futai, G.-H. Sun-Wada, S. Bourgoin, J.
1028 Casanova, A. Wildeman, S. Bechoua, D.A. Ausiello, D. Brown, and V. Marshansky. 2006. V-
1029 ATPase interacts with ARNO and Arf6 in early endosomes and regulates the protein
1030 degradative pathway. *Nature Cell Biology*. 8:124–136. doi:10.1038/ncb1348.

1031 Johnson, D.E., P. Ostrowski, V. Jaumouillé, and S. Grinstein. 2016. The position of lysosomes
1032 within the cell determines their luminal pH. *The Journal of cell biology*. 212:677–692.
1033 doi:10.1083/jcb.201507112.

1034 Kanai, F., H. Liu, S.J. Field, H. Akbary, T. Matsuo, G.E. Brown, L.C. Cantley, and M.B. Yaffe.
1035 2001. The PX domains of p47phox and p40phox bind to lipid products of PI(3)K. *Nat Cell*
1036 *Biol*. 3:675–678. doi:10.1038/35083070.

1037 Kawasaki-Nishi, S. 2001. The Amino-terminal Domain of the Vacuolar Proton-translocating
1038 ATPase a Subunit Controls Targeting and in Vivo Dissociation, and the Carboxyl-terminal
1039 Domain Affects Coupling of Proton Transport and ATP Hydrolysis. *Journal of Biological*
1040 *Chemistry*. 276:47411–47420. doi:10.1074/jbc.M108310200.

1041 Levin-Konigsberg, R., F. Montaño-Rendón, T. Keren-Kaplan, R. Li, B. Ego, S. Mylvaganam, J.E.
1042 DiCiccio, W.S. Trimble, M.C. Bassik, J.S. Bonifacino, G.D. Fairn, and S. Grinstein. 2019.
1043 Phagolysosome resolution requires contacts with the endoplasmic reticulum and
1044 phosphatidylinositol-4-phosphate signalling. *Nature Cell Biology*. 21:1234–1247.
1045 doi:10.1038/s41556-019-0394-2.

1046 Li, Q. 2004. A Syntaxin 1, G o, and N-Type Calcium Channel Complex at a Presynaptic Nerve
1047 Terminal: Analysis by Quantitative Immunocolocalization. *Journal of Neuroscience*. 24:4070–
1048 4081. doi:10.1523/JNEUROSCI.0346-04.2004.

1049 Liesche, C., K.S. Grußmayer, M. Ludwig, S. Wörz, K. Rohr, D.-P. Herten, J. Beaudouin, and R.
1050 Eils. 2015. Automated Analysis of Single-Molecule Photobleaching Data by Statistical
1051 Modeling of Spot Populations. *Biophysical Journal*. 109:2352–2362.
1052 doi:10.1016/j.bpj.2015.10.035.

1053 Loewen, C.J.R., and T.P. Levine. 2005. A Highly Conserved Binding Site in Vesicle-associated
1054 Membrane Protein-associated Protein (VAP) for the FFAT Motif of Lipid-binding Proteins.
1055 *Journal of Biological Chemistry*. 280:14097–14104. doi:10.1074/jbc.M500147200.

1056 Lukacs, G.L., O.D. Rotstein, and S. Grinstein. 1990. Phagosomal acidification is mediated by a
1057 vacuolar-type H(+)-ATPase in murine macrophages. *J Biol Chem*. 265:21099–21107.

1058 Maranda, B., D. Brown, S. Bourgoin, J.E. Casanova, P. Vinay, D.A. Ausiello, and V.
1059 Marshansky. 2001. Intra-endosomal pH-sensitive recruitment of the Arf-nucleotide exchange
1060 factor ARNO and Arf6 from cytoplasm to proximal tubule endosomes. *The Journal of*
1061 *biological chemistry*. 276:18540–18550. doi:10.1074/jbc.M011577200.

1062 Marshansky, V., J.L. Rubinstein, and G. Grüber. 2014. Eukaryotic V-ATPase: Novel structural
1063 findings and functional insights. *Biochimica et Biophysica Acta (BBA) - Bioenergetics*.
1064 1837:857–879. doi:10.1016/j.bbabio.2014.01.018.

1065 Martinez, I., S. Chakrabarti, T. Hellevik, J. Morehead, K. Fowler, and N.W. Andrews. 2000.
1066 Synaptotagmin VII regulates Ca(2+)-dependent exocytosis of lysosomes in fibroblasts. *The*
1067 *Journal of cell biology*. 148:1141–1149.

1068 Maxfield, F.R., and T.E. McGraw. 2004. Endocytic recycling. *Nat Rev Mol Cell Biol*. 5:121–132.
1069 doi:10.1038/nrm1315.

1070 Maxson, M.E., and S. Grinstein. 2014. The vacuolar-type H+-ATPase at a glance - more than a
1071 proton pump. *Journal of cell science*. 127:4987–4993.

1072 McGuire, C.M., M.P. Collins, G. Sun-Wada, Y. Wada, and M. Forgac. 2019. Isoform-specific
1073 gene disruptions reveal a role for the V-ATPase subunit a4 isoform in the invasiveness of
1074 4T1-12B breast cancer cells. *Journal of Biological Chemistry*. 294:11248–11258.
1075 doi:10.1074/jbc.RA119.007713.

1076 Mellman, I., R. Fuchs, and A. Helenius. 1986. Acidification of the Endocytic and Exocytic
1077 Pathways. *Annu. Rev. Biochem.* 55:663–700. doi:10.1146/annurev.bi.55.070186.003311.

1078 Merkulova, M., T.G. Păunescu, A. Azroyan, V. Marshansky, S. Breton, and D. Brown. 2015.
1079 Mapping the H + (V)-ATPase interactome: identification of proteins involved in trafficking,
1080 folding, assembly and phosphorylation. *Scientific reports*. 5:1–15. doi:10.1038/srep14827.

1081 Michel, V., Y. Licon-Munoz, K. Trujillo, M. Bisoffi, and K.J. Parra. 2013. Inhibitors of vacuolar
1082 ATPase proton pumps inhibit human prostate cancer cell invasion and prostate-specific
1083 antigen expression and secretion. *Int. J. Cancer*. 132:E1–E10. doi:10.1002/ijc.27811.

1084 Mullock, B.M., N.A. Bright, C.W. Fearon, S.R. Gray, and J. Luzio. 1998. Fusion of Lysosomes
1085 with Late Endosomes Produces a Hybrid Organelle of Intermediate Density and Is NSF
1086 Dependent. *The Journal of cell biology*. 140:591–601. doi:10.1083/jcb.140.3.591.

1087 Naufer, A., V.E.B. Hipolito, S. Ganesan, A. Prashar, V. Zaremberg, R.J. Botelho, and M.R.
1088 Terebiznik. 2018. pH of endophagosomes controls association of their membranes with
1089 Vps34 and PtdIns(3)P levels. *J Cell Biol*. 217:329–346. doi:10.1083/jcb.201702179.

1090 Ostrowski, P.P., G.D. Fairn, S. Grinstein, and D.E. Johnson. 2016. Cresyl violet: a superior
1091 fluorescent lysosomal marker. *Traffic*. 17:1313–1321. doi:10.1111/tra.12447.

1092 Parra, K.J., and P.M. Kane. 1998. Reversible Association between the V1and V0 Domains of
1093 Yeast Vacuolar H+-ATPase Is an Unconventional Glucose-Induced Effect. *Molecular and*
1094 *Cellular Biology*. 18:7064–7074.

1095 Poëa-Guyon, S., M.R. Ammar, M. Erard, M. Amar, A.W. Moreau, P. Fossier, V. Gleize, N.
1096 Vitale, and N. Morel. 2013. The V-ATPase membrane domain is a sensor of granular pH that
1097 controls the exocytotic machinery. *The Journal of cell biology*. 203:283–298.

1098 Ramirez, C., A.D. Hauser, E.A. Vucic, and D. Bar-Sagi. 2019. Plasma membrane V-ATPase
1099 controls oncogenic RAS-induced macropinocytosis. *Nature*. 576:1–21.

1100 Roberts, R.L., M.A. Barbieri, J. Ullrich, and P.D. Stahl. 2000. Dynamics of rab5 activation in
1101 endocytosis and phagocytosis. *Journal of Leukocyte Biology*. 68:627–632.

1102 Rocha, N., C. Kuijl, R. van der Kant, L. Janssen, D. Houben, H. Janssen, W. Zwart, and J.
1103 Neefjes. 2009. Cholesterol sensor ORP1L contacts the ER protein VAP to control Rab7-
1104 RILP-p150 Glued and late endosome positioning. *J Cell Biol*. 185:1209–1225.
1105 doi:10.1083/jcb.200811005.

1106 Saftig, P., and J. Klumperman. 2009. Lysosome biogenesis and lysosomal membrane proteins:
1107 trafficking meets function. *Nat Rev Mol Cell Biol*. 10:623–635. doi:10.1038/nrm2745.

1108 Saw, N.M.N., S.-Y.A. Kang, L. Parsaud, G.A. Han, T. Jiang, K. Grzegorczyk, M. Surkont, G.-H.
1109 Sun-Wada, Y. Wada, L. Li, and S. Sugita. 2011. Vacuolar H(+)-ATPase subunits Voa1 and
1110 Voa2 cooperatively regulate secretory vesicle acidification, transmitter uptake, and storage.
1111 *Molecular Biology of the Cell*. 22:3394–3409. doi:10.1091/mbc.E11-02-0155.

1112 Sharma, S., and S. Wilkens. 2017. Biolayer interferometry of lipid nanodisc-reconstituted yeast
1113 vacuolar H+ -ATPase. *Protein Science*. 26:1070–1079. doi:10.1002/pro.3143.

1114 Sun-Wada, G.H., T. Toyomura, Y. Murata, A. Yamamoto, M. Futai, and Y. Wada. 2006. The a3
1115 isoform of V-ATPase regulates insulin secretion from pancreatic -cells. *Journal of cell*
1116 *science*. 119:4531–4540. doi:10.1242/jcs.03234.

1117 Suresh, B., A. Saminathan, K. Chakraborty, C. Cui, L. Becker, and Y. Krishnan. 2020. Tubular
1118 lysosomes harbor active ion gradients and poise macrophages for phagocytosis. *bioRxiv*.
1119 doi:10.1101/2020.12.05.413229.

1120 Swanson, J., B. Yirinec, E. Burke, A. Bushnell, and S.C. Silverstein. 1986. Effect of alterations
1121 in the size of the vacuolar compartment on pinocytosis in J774.2 macrophages. *Journal of*
1122 *cellular physiology*. 128:195–201. doi:10.1002/jcp.1041280209.

1123 Tabke, K., A. Albertmelcher, O. Vitavska, M. Huss, H.-P. Schmitz, and H. Wieczorek. 2014.
1124 Reversible disassembly of the yeast V-ATPase revisited under in vivo conditions. *Biochem.*
1125 *J*. 462:185–197. doi:10.1042/BJ20131293.

1126 Takamori, S., M. Holt, K. Stenius, E.A. Lemke, M. Grønborg, D. Riedel, H. Urlaub, S. Schenck,
1127 B. Brügger, P. Ringler, S.A. Müller, B. Rammner, F. Gräter, J.S. Hub, B.L. De Groot, G.
1128 Mieskes, Y. Moriyama, J. Klingauf, H. Grubmüller, J. Heuser, F. Wieland, and R. Jahn. 2006.
1129 Molecular Anatomy of a Trafficking Organelle. *Cell*. 127:831–846.
1130 doi:10.1016/j.cell.2006.10.030.

1131 Teruel, M.N., T.A. Blanpied, K. Shen, G.J. Augustine, and T. Meyer. 1999. A versatile
1132 microporation technique for the transfection of cultured CNS neurons. *J Neurosci Methods*.
1133 93:37–48. doi:10.1016/s0165-0270(99)00112-0.

1134 Toei, M., R. Saum, and M. Forgac. 2010. Regulation and isoform function of the V-ATPases.
1135 *Biochemistry*. 49:4715–4723. doi:10.1021/bi100397s.

1136 Uchida, E., Y. Ohsumi, and Y. Anraku. 1985. Purification and properties of H+-translocating,
1137 Mg2+-adenosine triphosphatase from vacuolar membranes of Saccharomyces cerevisiae.
1138 *The Journal of biological chemistry*. 260:1090–1095. doi:10.1016/S0021-9258(20)71211-1.

1139 Vasanthakumar, T., S.A. Bueler, D. Wu, V. Beilsten-Edmands, C.V. Robinson, and J.L.
1140 Rubinstein. 2019. Structural comparison of the vacuolar and Golgi V-ATPases from
1141 Saccharomyces cerevisiae. *Proceedings of the National Academy of Sciences*. 116:7272–
1142 7277. doi:10.1073/pnas.1814818116.

1143 Vieira, O.V., R.J. Botelho, L. Rameh, S.M. Brachmann, T. Matsuo, H.W. Davidson, A.
1144 Schreiber, J.M. Backer, L.C. Cantley, and S. Grinstein. 2001. Distinct roles of class I and
1145 class III phosphatidylinositol 3-kinases in phagosome formation and maturation. *The Journal*
1146 *of cell biology*. 155:19–25.

1147 Voss, M., O. Vitavska, B. Walz, H. Wieczorek, and O. Baumann. 2007. Stimulus-induced
1148 Phosphorylation of Vacuolar H+-ATPase by Protein Kinase A. *Journal of Biological*
1149 *Chemistry*. 282:33735–33742. doi:10.1074/jbc.M703368200.

1150 Webb, B.A., F.M. Aloisio, R.A. Charafeddine, J. Cook, T. Wittmann, and D.L. Barber. 2021.
1151 pHLARE: a new biosensor reveals decreased lysosome pH in cancer cells. *Mol Biol Cell*.
1152 32:131–142. doi:10.1091/mbc.E20-06-0383.

1153 Wijdeven, R.H., H. Janssen, L. Nahidiazar, L. Janssen, K. Jalink, I. Berlin, and J. Neefjes. 2016.
1154 Cholesterol and ORP1L-mediated ER contact sites control autophagosome transport and
1155 fusion with the endocytic pathway. *Nature Communications*. 7:1–14.

1156 Xu, L., X. Shen, A. Bryan, S. Banga, M.S. Swanson, and Z.-Q. Luo. 2010. Inhibition of Host
1157 Vacuolar H+-ATPase Activity by a Legionella pneumophila Effector. *PLOS Pathogens*.
1158 6:e1000822. doi:10.1371/journal.ppat.1000822.

1159 Xu, T., Q. Gan, B. Wu, M. Yin, J. Xu, X. Shu, and J. Liu. 2020. Molecular Basis for PI(3,5)P2
1160 Recognition by SNX11, a Protein Involved in Lysosomal Degradation and Endosome
1161 Homeostasis Regulation. *Journal of Molecular Biology*. 432:4750–4761.
1162 doi:10.1016/j.jmb.2020.06.010.

1163 Yajima, S., M. Kubota, T. Nakakura, T. Hasegawa, N. Katagiri, H. Tomura, Y. Sasayama, M.
1164 Suzuki, and S. Tanaka. 2007. Cloning and Expression of Vacuolar Proton-Pumping ATPase
1165 Subunits in the Follicular Epithelium of the Bullfrog Endolymphatic Sac. *Zoological Science*.
1166 24:147–157. doi:10.2108/zsj.24.147.

1167 Yordanov, T.E., V.E.B. Hipolito, G. Liebscher, G.F. Vogel, T. Stasyk, C. Herrmann, S. Geley, D.
1168 Teis, R.J. Botelho, M.W. Hess, and L.A. Huber. 2019. Biogenesis of lysosome-related
1169 organelles complex-1 (BORC) regulates late endosomal/lysosomal size through PIKfyve-
1170 dependent phosphatidylinositol-3,5-bisphosphate. *Traffic (Copenhagen, Denmark)*. 20:674–
1171 696. doi:10.1111/tra.12679.

1172 Zhao, J., S. Benlekbir, and J.L. Rubinstein. 2015. Electron cryomicroscopy observation of
1173 rotational states in a eukaryotic V-ATPase. *Nature*. 521:241–245. doi:10.1038/nature14365.

1174 Zhao, J., K. Beyrakhova, Y. Liu, C.P. Alvarez, S.A. Bueler, L. Xu, C. Xu, M.T. Boniecki, V.
1175 Kanelis, Z.-Q. Luo, M. Cygler, and J.L. Rubinstein. 2017. Molecular basis for the binding and
1176 modulation of V-ATPase by a bacterial effector protein. *PLOS Pathogens*. 13:e1006394.
1177 doi:10.1371/journal.ppat.1006394.

1178 Zoncu, R., L. Bar-Peled, A. Efeyan, S. Wang, Y. Sancak, and D.M. Sabatini. 2011. mTORC1
1179 Senses Lysosomal Amino Acids Through an Inside-Out Mechanism That Requires the
1180 Vacuolar H+-ATPase. *Science*. 334:678–683. doi:10.1126/science.1207056.

1181

Figure 1

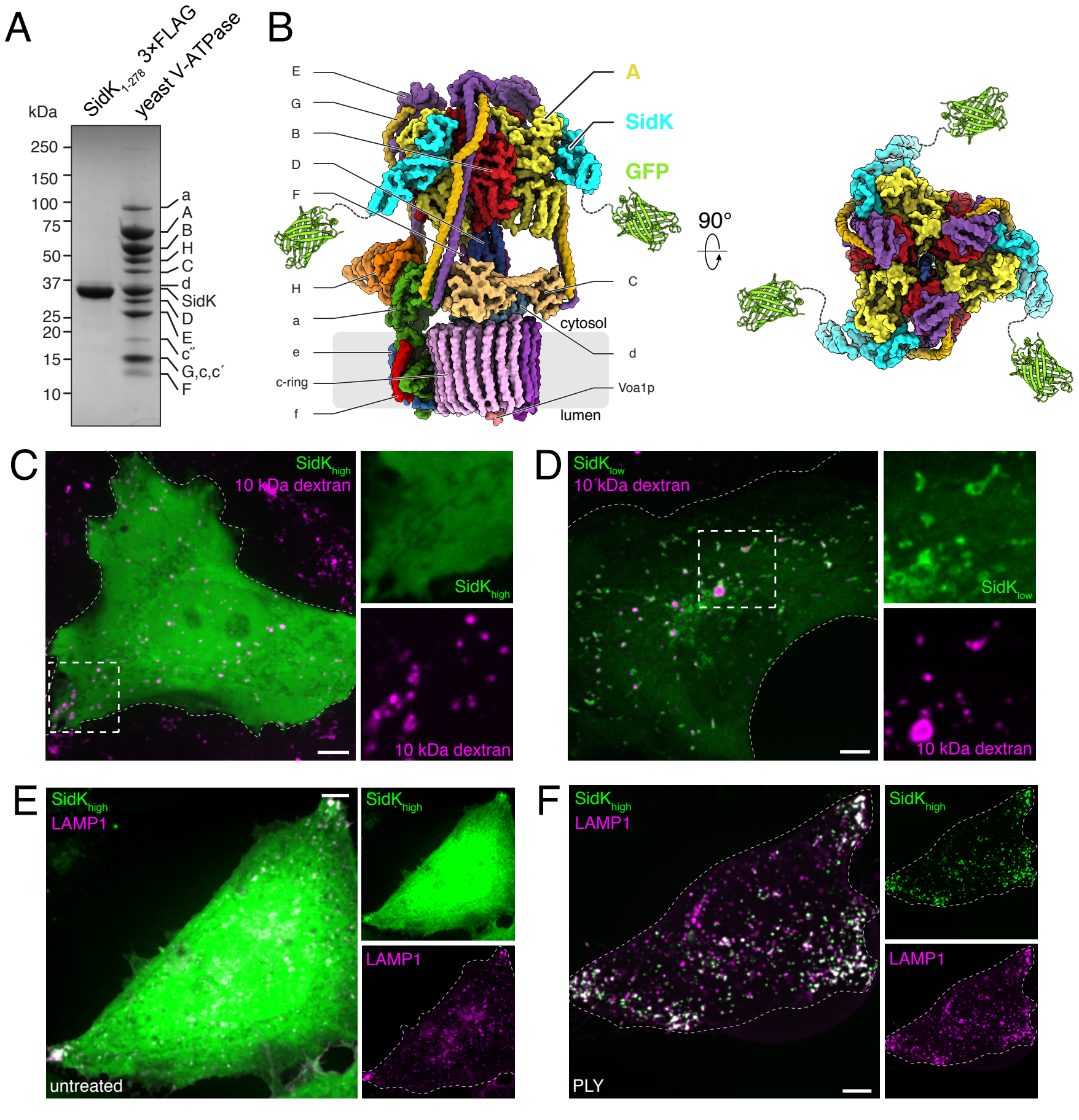
A
SidK1-278 3xFLAG
yeast V-ATPase
kDa
250
150
100
75
50
37
25
20
15
10
a
A
B
H
C
d
SidK
D
E
c˝
G,c,c´
F
B
E
G
B
D
F
H
a
e
c-ring
f
A
SidK
GFP
C
cytosol
d
Voa1p
lumen
90°
C
SidKhigh
10 kDa dextran
SidKhigh
10 kDa dextran
D
SidKlow
10 kDa dextran
SidKlow
10 kDa dextran
E
SidKhigh
LAMP1
untreated
SidKhigh
LAMP1
F
SidKhigh
LAMP1
PLY
SidKhigh
LAMP1

Figure 2

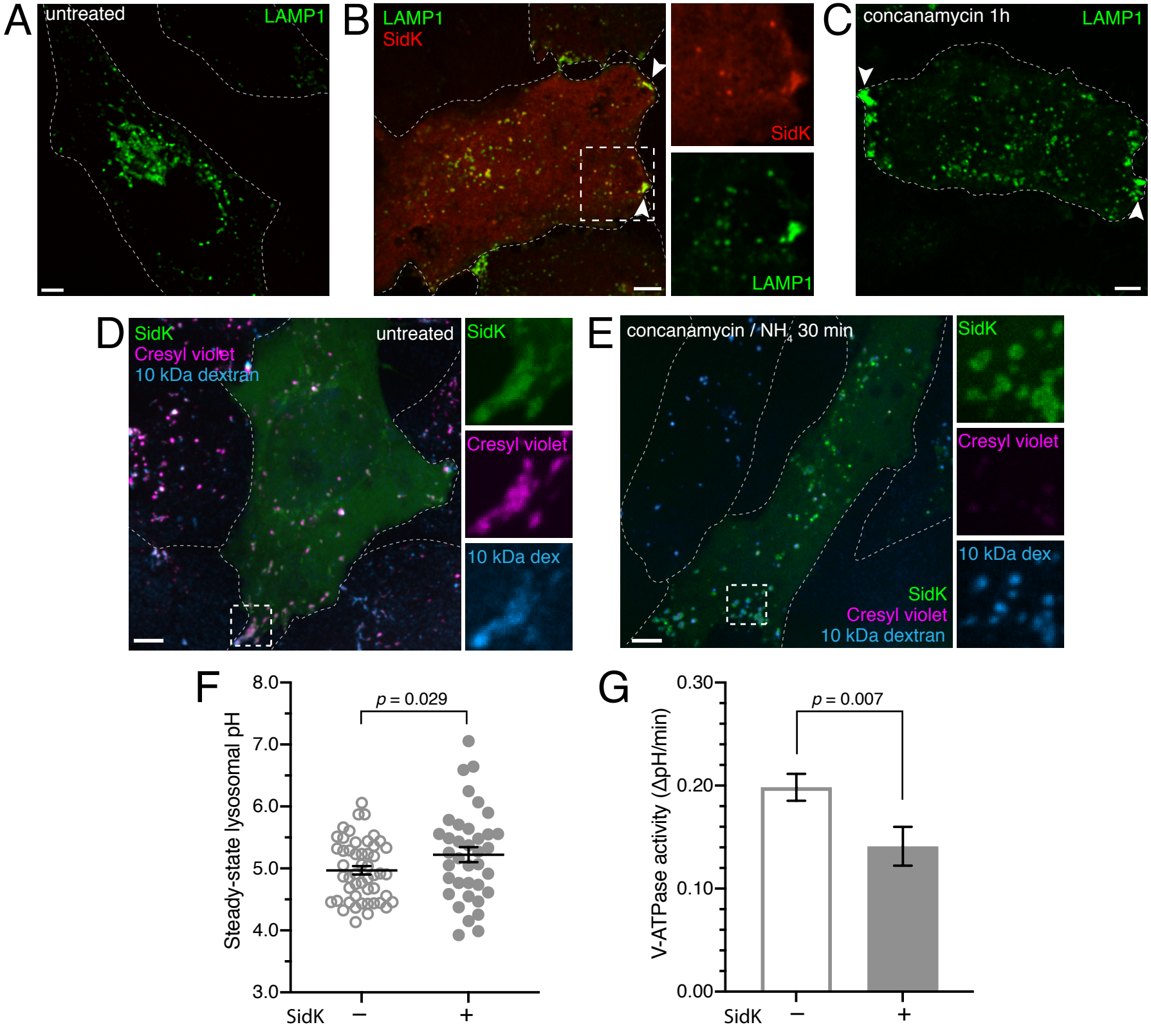
A
untreated
LAMP1
B
LAMP1
SidK
SidK
LAMP1
C
concanamycin 1h
LAMP1
D
SidK
Cresyl violet
10 kDa dextran
untreated
SidK
Cresyl violet
10 kDa dex
E
concanamycin / NH4 30 min
SidK
Cresyl violet
10 kDa dextran
SidK
Cresyl violet
10 kDa dex
F
Steady-state lysosomal pH
8.0
7.0
6.0
5.0
4.0
3.0
p = 0.029
SidK
–
+
G
V-ATPase activity (ΔpH/min)
0.30
0.20
0.10
0.00
p = 0.007
SidK
–
+

Figure 3

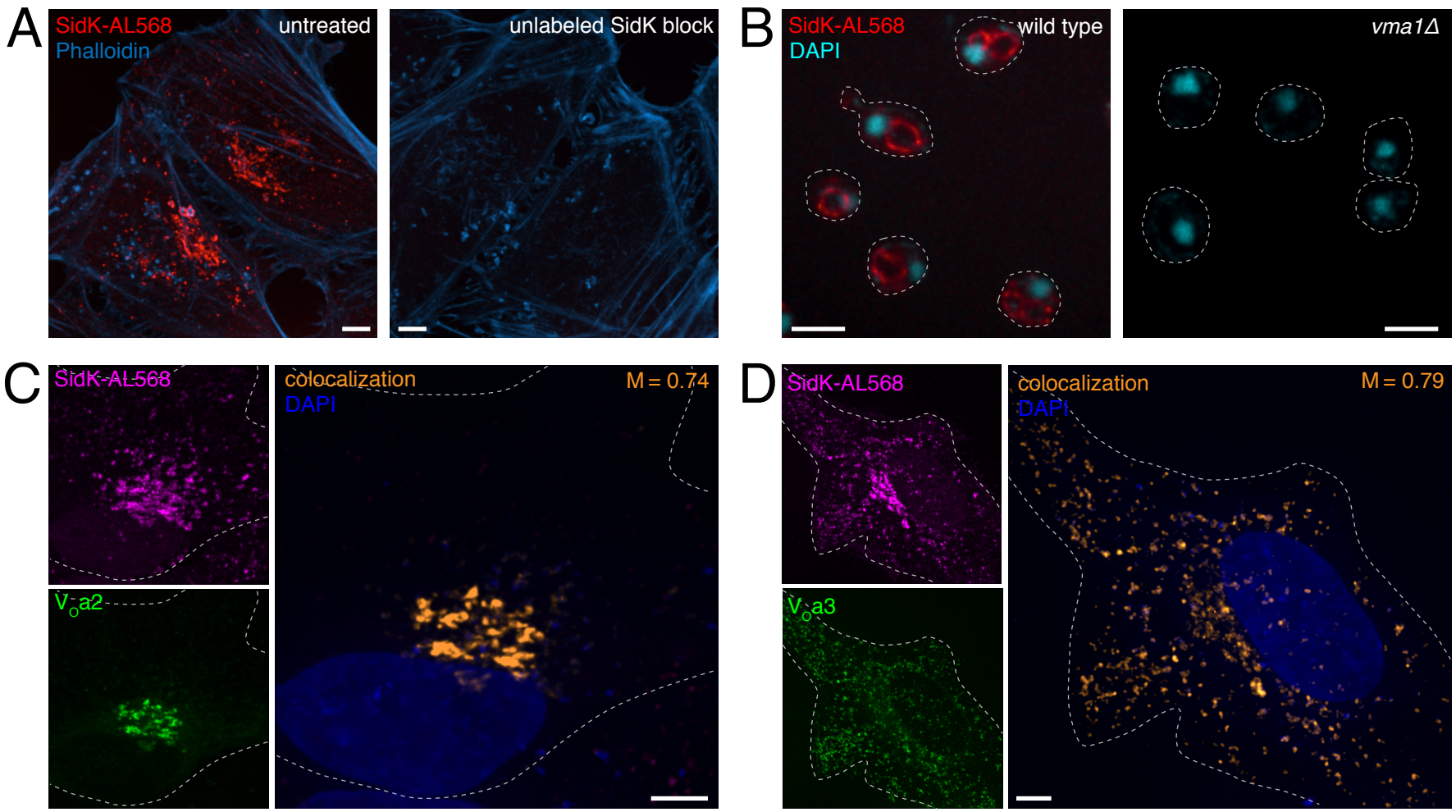
A
SidK-AL568
Phalloidin
untreated
unlabeled SidK block
B
SidK-AL568
DAPI
wild type
vma1Δ
C
SidK-AL568
Vo a2
colocalization
DAPI
M = 0.74
D
SidK-AL568
Vo a3
colocalization
DAPI
M = 0.79

Figure 4

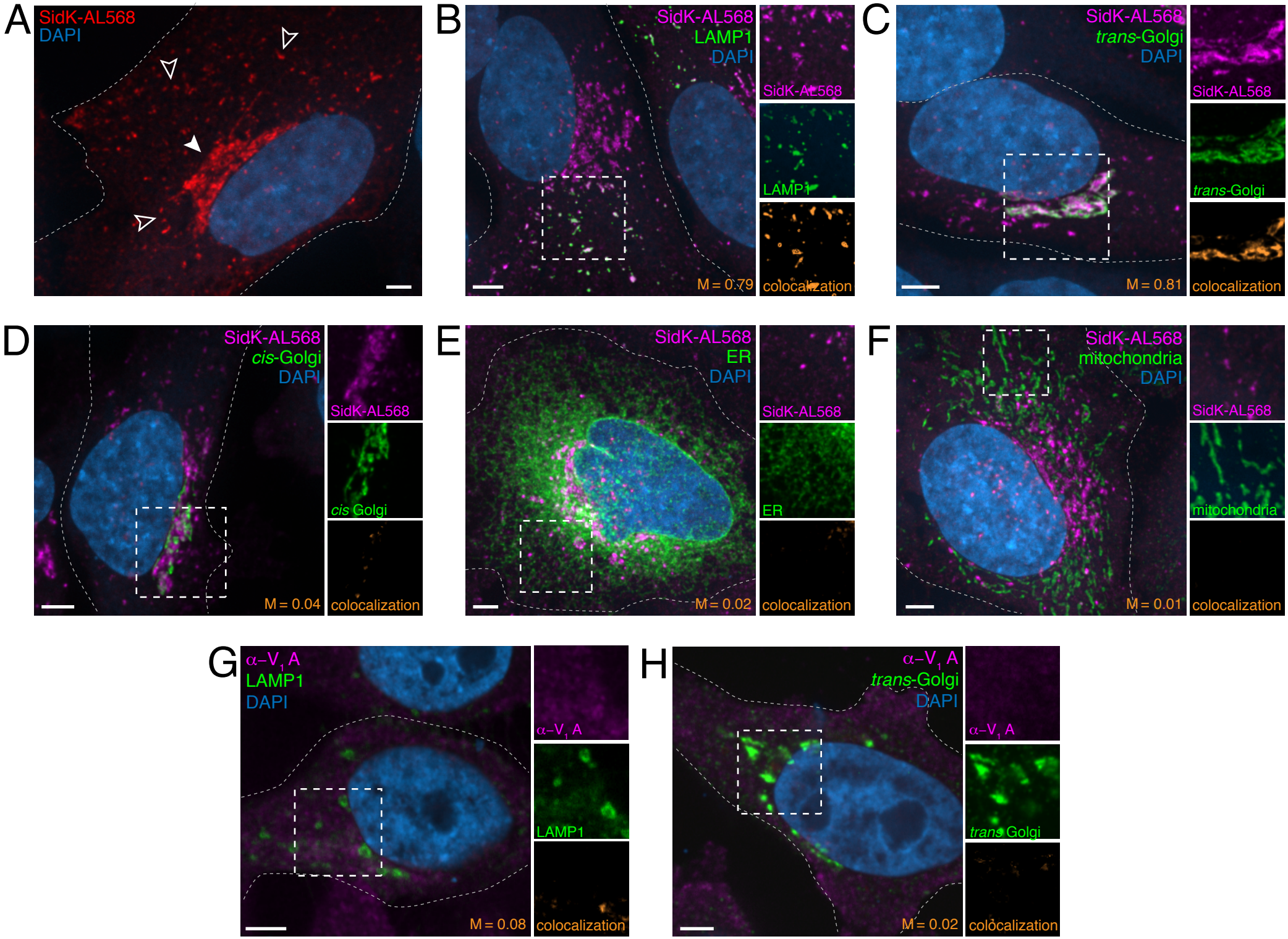
A
SidK-AL568
DAPI
B
SidK-AL568
LAMP1
DAPI
SidK-AL568
LAMP1
M = 0.79
colocalization
C
SidK-AL568
trans-Golgi
DAPI
SidK-AL568
trans-Golgi
M = 0.81
colocalization
D
SidK-AL568
cis-Golgi
DAPI
SidK-AL568
cis Golgi
M = 0.04
colocalization
E
SidK-AL568
ER
DAPI
SidK-AL568
ER
M = 0.02
colocalization
F
SidK-AL568
mitochondria
DAPI
SidK-AL568
mitochondria
M = 0.01
colocalization
G
α–V1 A
LAMP1
DAPI
α–V1 A
LAMP1
M = 0.08
colocalization
H
α–V1 A
trans-Golgi
DAPI
α–V1 A
trans Golgi
M = 0.02
colocalization

Figure 5

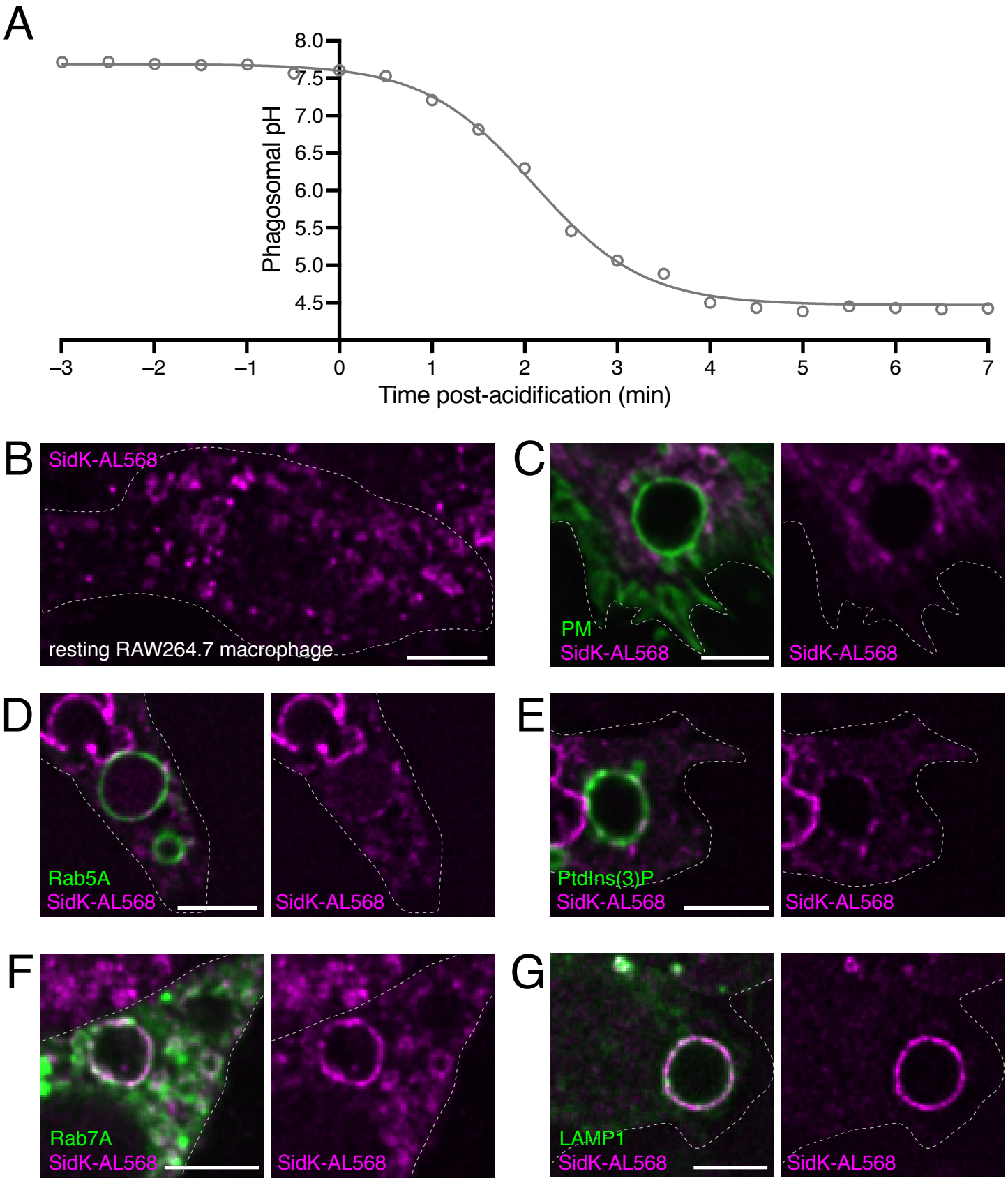

Figure 5

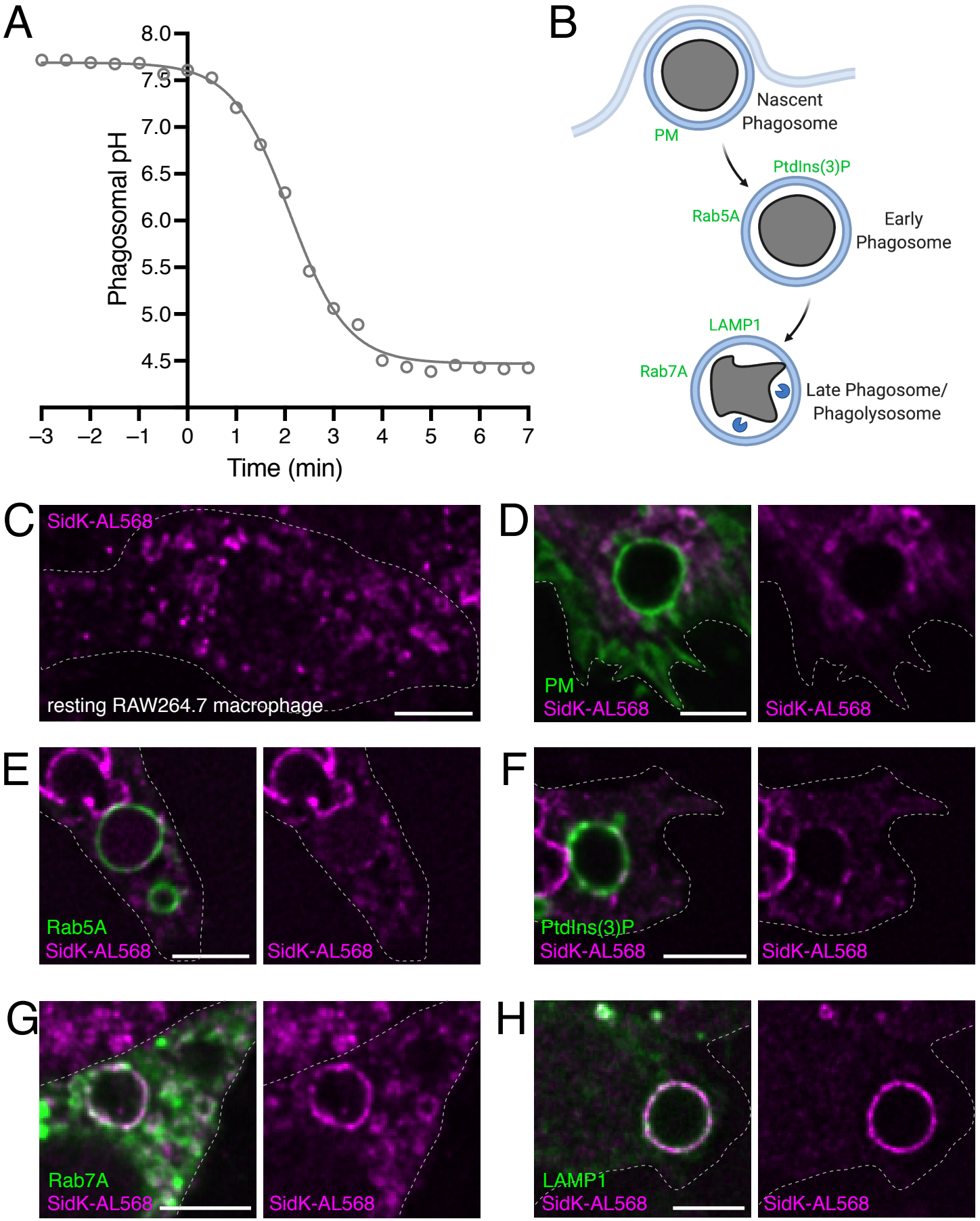

Figure 5

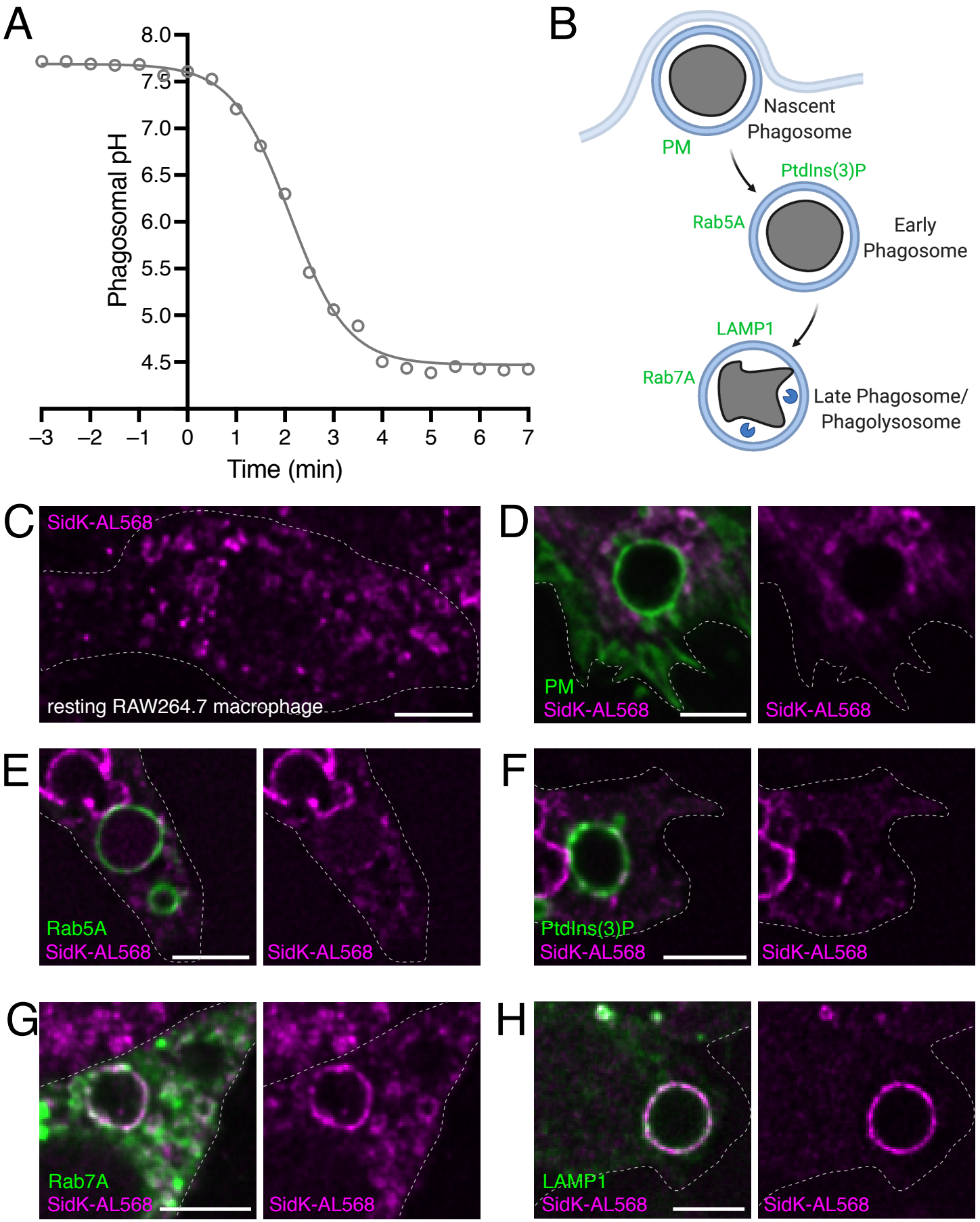

Figure 6

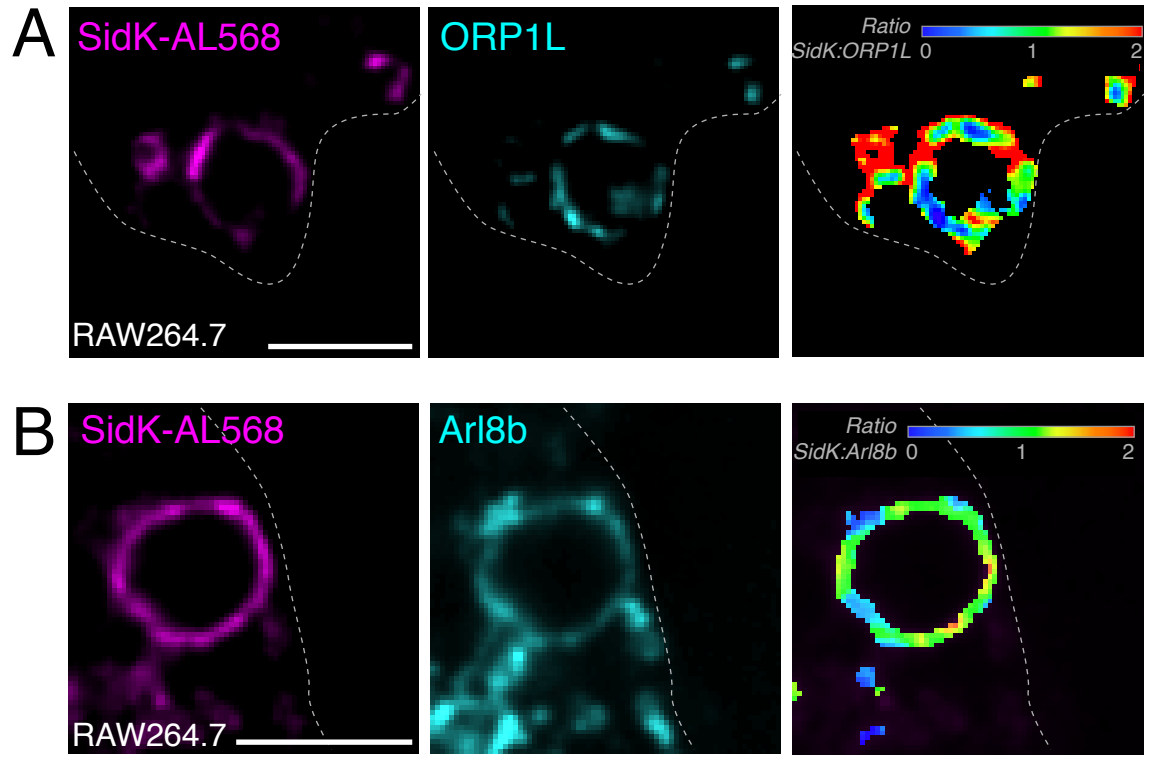
A
SidK-AL568
ORP1L
Ratio
SidK:ORP1L 0
1
2
RAW264.7
B
SidK-AL568
Arl8b
Ratio
SidK:Arl8b 0
1
2
RAW264.7

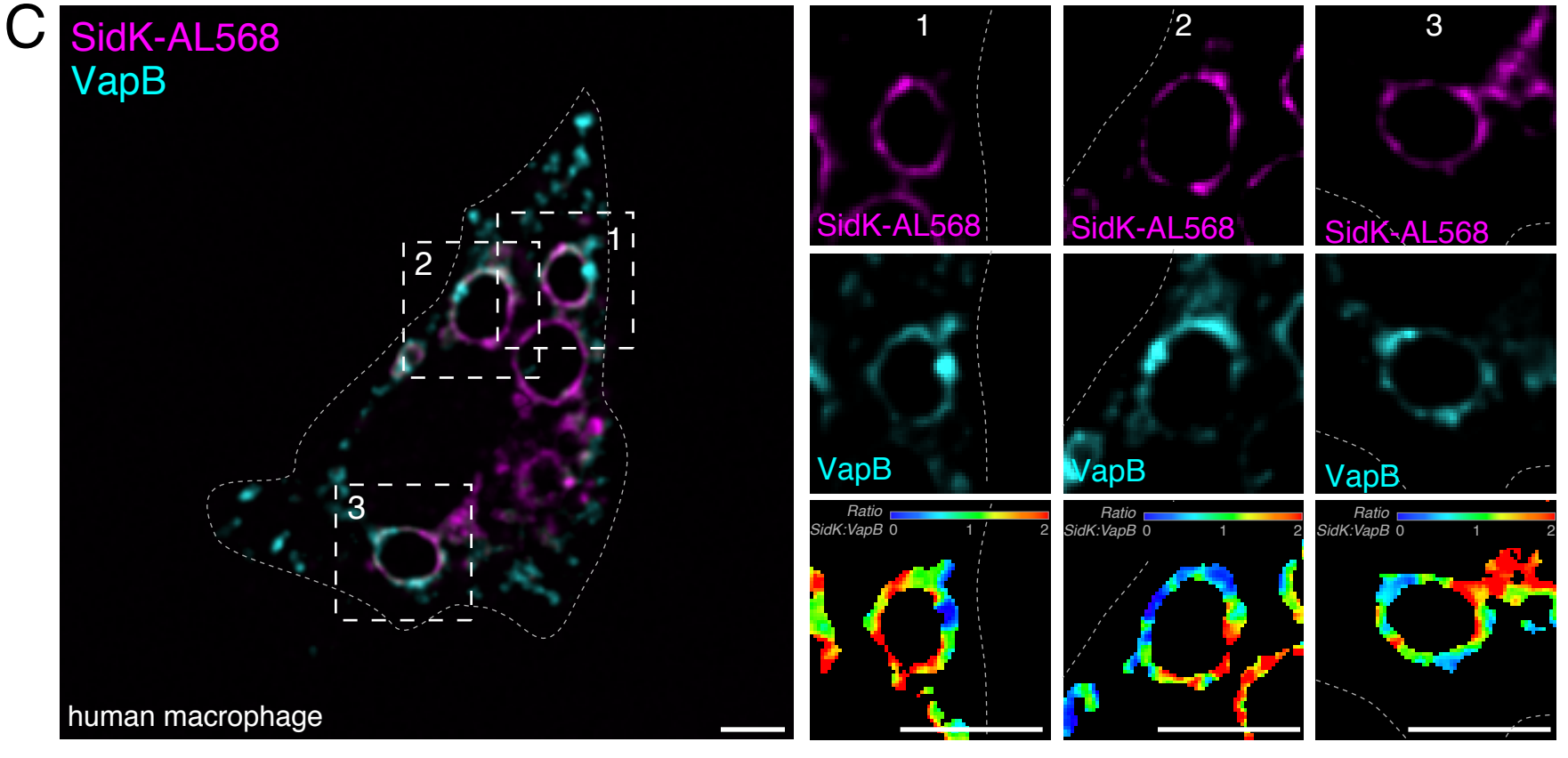
C
SidK-AL568
VapB
1
2
3
human macrophage
1
2
3
SidK-AL568
SidK-AL568
SidK-AL568
VapB
VapB
VapB
Ratio
SidK:VapB 0
1
2
Ratio
SidK:VapB 0
1
2
Ratio
SidK:VapB 0
1
2

Figure 7

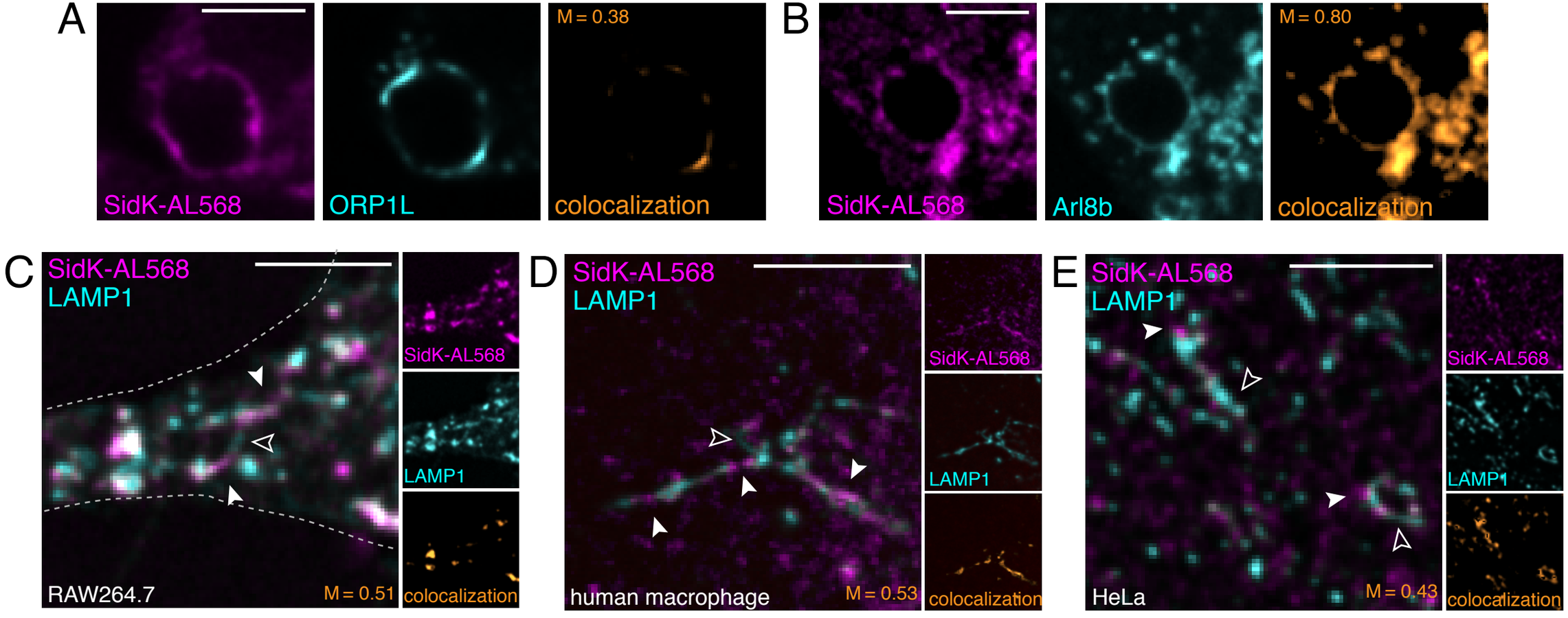
A
SidK-AL568
ORP1L
M = 0.38
colocalization
B
SidK-AL568
Arl8b
M = 0.80
colocalization
C
SidK-AL568
LAMP1
RAW264.7
M = 0.51
SidK-AL568
LAMP1
colocalization
D
SidK-AL568
LAMP1
human macrophage
M = 0.53
SidK-AL568
LAMP1
colocalization
E
SidK-AL568
LAMP1
HeLa
M = 0.43
SidK-AL568
LAMP1
colocalization

Figure 8

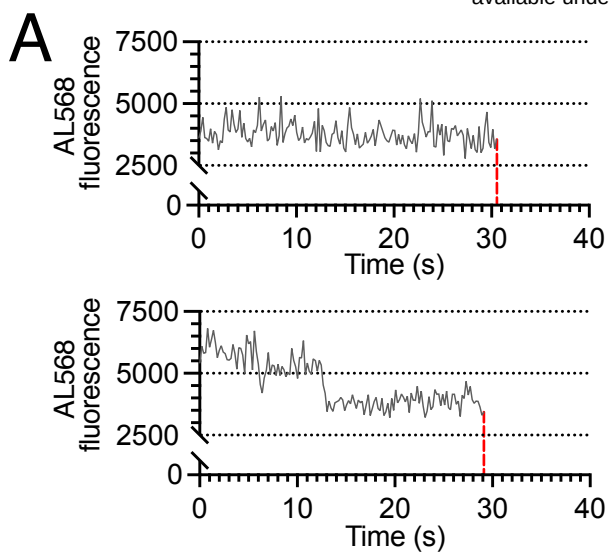

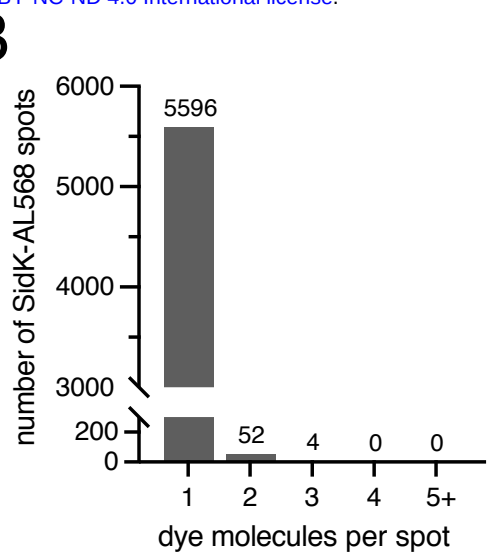

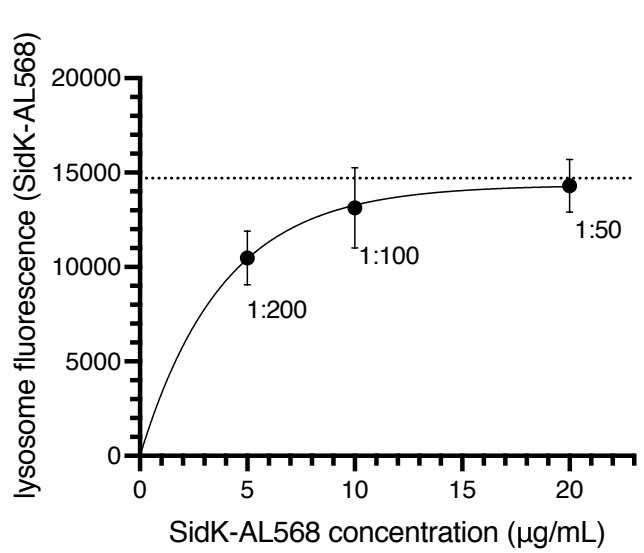

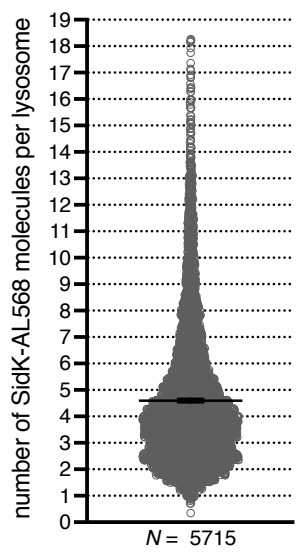

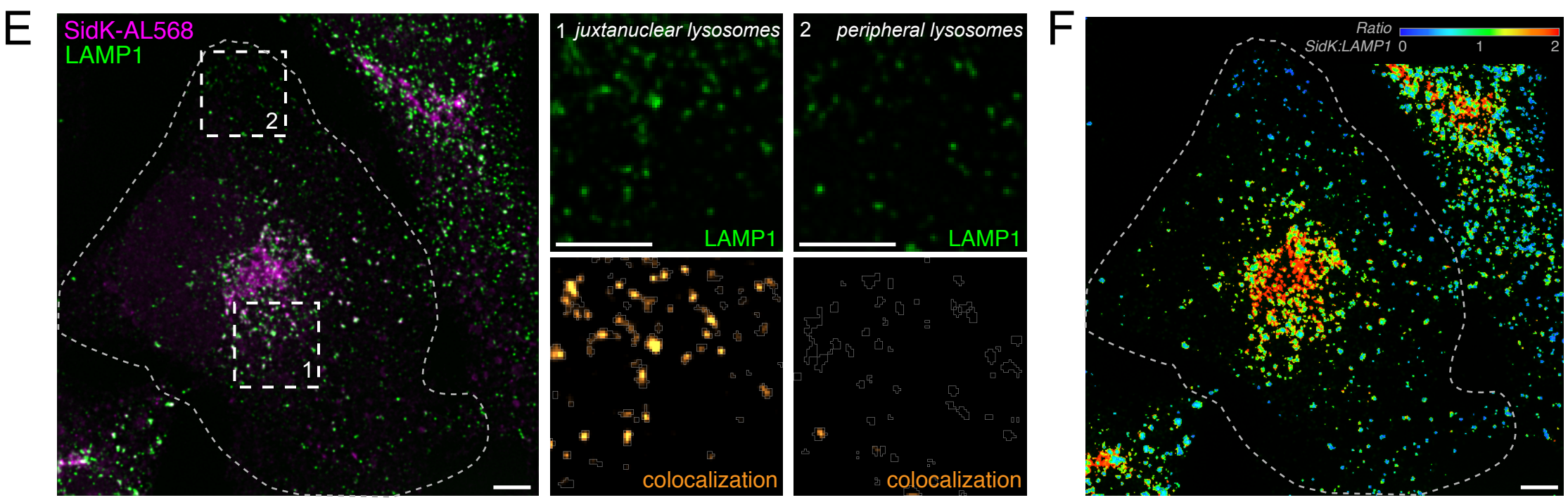

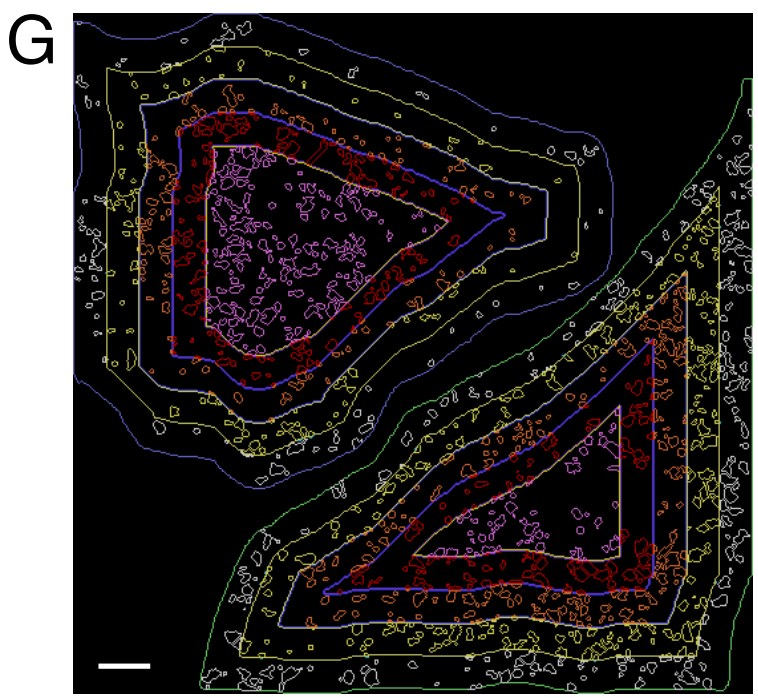

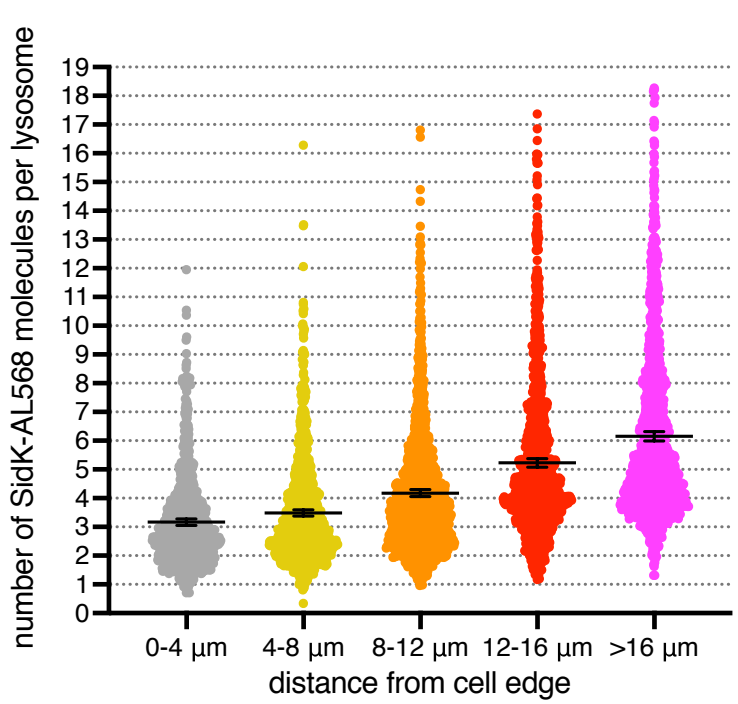

Figure S1

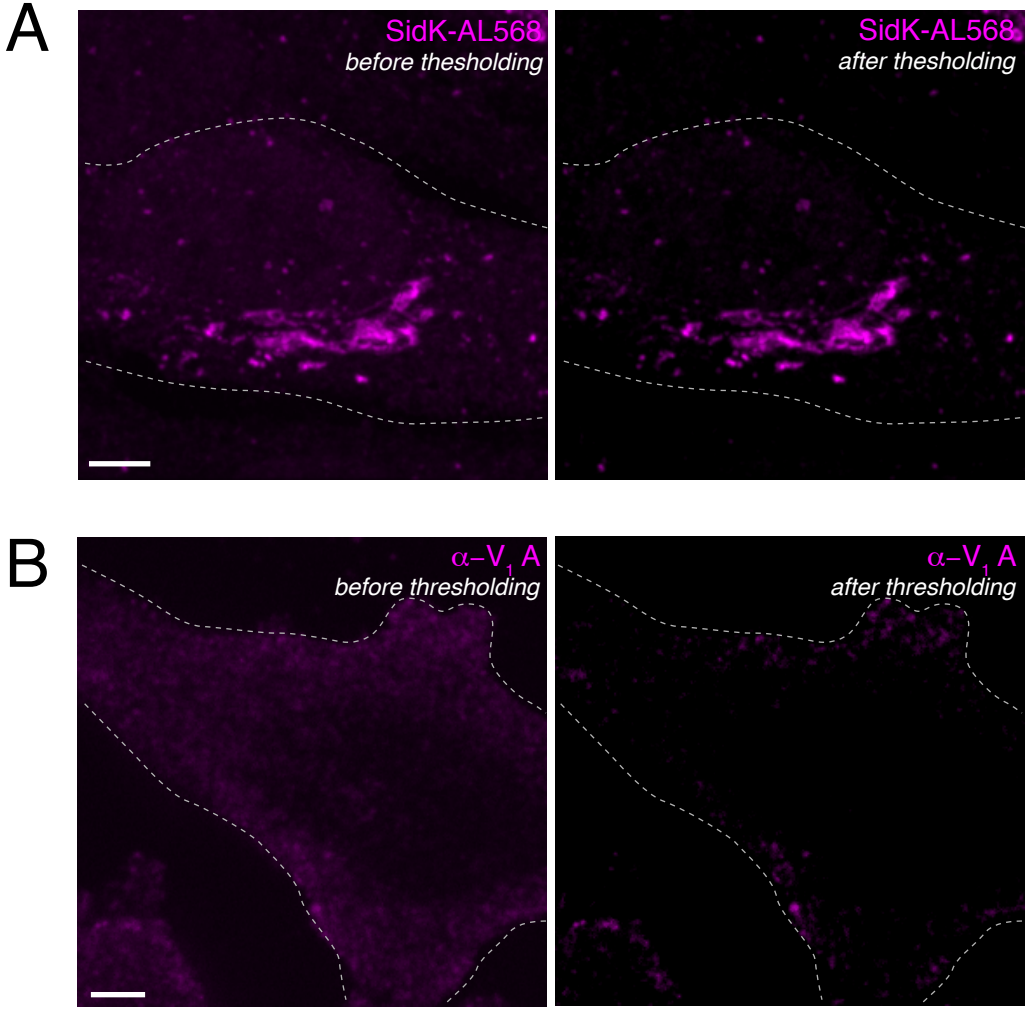
A
SidK-AL568
before thesholding
SidK-AL568
after thesholding
B
α–V1 A
before thresholding
α–V1 A
after thresholding